Published for SISSA by Springer
Received: December 27, 2021
Accepted: March 29, 2022
Published: April 21, 2022

Hadron collider probes of the quartic couplings of gluons to the photon and Z boson

John Ellis,[a,b,c] **Shao-Feng Ge**[d,e] **and Kai Ma**[f,g,h,d]

[a] *Department of Physics, King's College London, Strand, London WC2R 2LS, U.K.*
[b] *Theoretical Physics Department, CERN, Esplanade des Particules 1, CH-1211 Geneva 23, Switzerland*
[c] *National Institute of Chemical Physics & Biophysics, Rävala 10, 10143 Tallinn, Estonia*
[d] *Tsung-Dao Lee Institute & School of Physics and Astronomy, Shanghai Jiao Tong University, Shanghai 200240, China*
[e] *Key Laboratory for Particle Astrophysics and Cosmology (MOE) & Shanghai Key Laboratory for Particle Physics and Cosmology, Shanghai Jiao Tong University, Shanghai 200240, China*
[f] *School of Fundamental Physics and Mathematical Science, Hangzhou Institute for Advanced Study, UCAS, Hangzhou 310024, Zhejiang, China*
[g] *International Centre for Theoretical Physics Asia-Pacific, Beijing/Hangzhou, China*
[h] *Department of Physics, Shaanxi University of Technology, Hanzhong 723000, Shaanxi, China*

E-mail: John.Ellis@cern.ch, gesf@sjtu.edu.cn, makai@ucas.ac.cn

Abstract: We explore the experimental sensitivities of measuring the $gg \to Z\gamma$ process at the LHC to the dimension-8 quartic couplings of gluon pairs to the Z boson and photon, in addition to comparing them with the analogous sensitivities in the $gg \to \gamma\gamma$ process. These processes can both receive contributions from 4 different CP-conserving dimension-8 operators with distinct Lorentz structures that contain a pair of gluon field strengths, $\hat{G}^a_{\mu\nu}$, and a pair of electroweak SU(2) gauge field strengths, $W^i_{\mu\nu}$, as well as 4 similar operators containing a pair of $\hat{G}^a_{\mu\nu}$ and a pair of U(1) gauge field strengths, $B_{\mu\nu}$. We calculate the scattering angular distributions for $gg \to Z\gamma$ and the $Z \to \bar{f}f$ decay angular distributions for these 4 Lorentz structures, as well as the Standard Model background. We analyze the sensitivity of ATLAS measurements of the $Z(\to \ell^+\ell^-, \bar{\nu}\nu, \bar{q}q)\gamma$ final states with integrated luminosities up to 139 fb^{-1} at $\sqrt{s} = 13$ TeV, showing that they exclude values $\lesssim 2$ TeV for the dimension-8 operator scales, and compare the $Z\gamma$ sensitivity with that of an ATLAS measurement of the $\gamma\gamma$ final state. We present combined $Z\gamma$ and $\gamma\gamma$ constraints on the scales of dimension-8 SMEFT operators and $\gamma\gamma$ constraints on the nonlinearity scale of the Born-Infeld extension of the Standard Model. We also estimate the sensitivities to dimension-8 operators of experiments at possible future proton-proton colliders with centre-of-mass energies of 25, 50 and 100 TeV, and discuss possible measurements of the Z spin and angular correlations.

Keywords: Phenomenological Models

ArXiv ePrint: 2112.06729

https://doi.org/10.1007/JHEP04(2022)123

Contents

JHEP04(2022)123

1 Introduction

In the Standard Model (SM) of particle physics, the triple and quartic gauge couplings are fixed by gauge symmetry. Measuring these couplings can test not only whether the gauge symmetry is realized linearly or nonlinearly in the low-energy effective theory of the electroweak symmetry-breaking sector [1] but also provide an interesting way of looking for possible new physics beyond the SM [2, 3]. Hence the search for anomalous gauge couplings is one of the priority measurements for LHC and possible future colliders. Many studies have been made of the present and prospective experimental sensitivities to triple gauge couplings (TGC) and quartic gauge couplings (QGC) between electroweak $\mathrm{SU}(2)_L \times \mathrm{U}(1)_Y$ gauge bosons. Quartic couplings between these and the $\mathrm{SU}(3)_c$ gluons are absent in the Standard Model (SM), but are also allowed in the Standard Model Effective Field Theory (SMEFT) at the level of dimension-8 operators. These have not been studied to the same extent as dimension-6 SMEFT operators (see [4, 5] and references therein), though there have recently been studies of dimension-8 operators that generate QGCs between photons [6] and between photons and gluons [7], as well as those that generate neutral TGCs [8, 9].

The dimension-8 operators that generate QGCs also arise from loop diagrams in the SM, via extensions of the original calculations by Heisenberg and Euler [10, 11], and may be generated by the exchanges of massive axion, dilaton or spin-2 resonances. One particular combination of dimension-8 interactions arises in Born-Infeld theory [12–15]:

$$\mathcal{L}_{\mathrm{BISM}} = \beta^2 \left[1 - \sqrt{1 + \sum_{\lambda=1}^{12} \frac{F^{\lambda}_{\mu\nu} F^{\lambda,\mu\nu}}{2\beta^2} - \left(\sum_{\lambda=1}^{12} \frac{F^{\lambda}_{\mu\nu} \widetilde{F}^{\lambda,\mu\nu}}{4\beta^2} \right)^2} \right] , \tag{1.1}$$

where the index λ runs over the 12 generators of the SM $\mathrm{SU}(3)_c \times \mathrm{SU}(2)_L \times \mathrm{U}(1)_Y$ gauge groups. The parameter $\beta \equiv M^2$ is the Born-Infeld nonlinearity scale associated with high-scale physics. The Born-Infeld extension of SM (BISM) may have deep roots in M-theory-inspired models, where it is related to the separation between branes [14]. Since all the SM gauge group factors appear in eq. (1.1), it generates quartic couplings of gluons to electroweak gauge bosons (gluonic QGCs, gQGCs) [7].

The cleanest strategy for searching for the photonic and gluonic QGC operators is to study processes that do not receive SM or dimension-6 SMEFT contributions. For example, the diphoton final state generated by light-by-light scattering, $\gamma\gamma \to \gamma\gamma$, provides a very clean probe of the photonic QGCs [6]. A first LHC constraint on light-by-light scattering was provided by an ATLAS measurement in heavy-ion collisions [16] (see also [17]). Its rate was found to be consistent with the Heisenberg-Euler prediction [10, 11], allowing lower limits $\mathcal{O}(100)$ GeV to be set on the scale of a Born-Infeld extension of QED and other possible dimension-8 SMEFT interactions [6]. Recently, the CMS and TOTEM collaborations updated the lower limits on the basis of a search for the exclusive production of high-mass $\gamma\gamma$ final states in pp collisions at the LHC [18]. Diphoton final states generated by gluon-gluon scattering, $gg \to \gamma\gamma$, provide clean probes of gluonic QGCs [7], and the 13 TeV data of ATLAS with 37 fb^{-1} [19] enabled lower limits $\gtrsim 1$ TeV to be placed on the scales of the gQGC operators [7].

In this paper we study in more detail the present and prospective future experimental sensitivities to the gQGC operators involving gluons and pairs of neutral electroweak bosons, Z and γ. We present a first analysis of $gg \to Z\gamma$ scattering and compare this with its $gg \to \gamma\gamma$ counterpart. We analyze ATLAS measurements of $Z\gamma$ production followed by $Z \to \ell^+\ell^-$ [20], $\bar{\nu}\nu$ [21] and $\bar{q}q$ [22] decays, with up to 139 fb^{-1} of luminosity at $\sqrt{s} = 13$ TeV. The scale of the dimension-8 gQGC operators can be constrained up to $\gtrsim 2$ TeV, higher than obtained in the updated analysis of the diphoton channel that we also present in the current paper. However, we also show that whereas measurements of the $Z\gamma$ final state do not constrain the BISM scale, the $\gamma\gamma$ process constrains its scale to $\gtrsim 5$ TeV. Interestingly, we note that a combination of measurements of the $Z\gamma$ and $\gamma\gamma$ final states could in principle disentangle the contribution of different operators. Finally we display the combined sensitivities of the $Z\gamma$ and $\gamma\gamma$ channels, and show how the sensitivities to dimension-8 operators could be increased in the future by measurements at possible proton-proton colliders with centre-of-mass energies of 25, 50 and 100 TeV.

The structure of the paper is as follows. Section 2 reviews the dimension-8 gQGC operators, especially those relevant to the associated production of Z and γ, as well as $\gamma\gamma$

JHEP04(2022)123

pair-production. Then section 3 studies the kinematics and differential cross sections of the $gg \to Z\gamma$ process at the LHC. In particular, we show how the unitary constraint can be implemented consistently. Following these preparations, we investigate the experimental constraints on the gQGC operators at the LHC in section 4 and future colliders in section 5. Then, in section 6 we present the helicity amplitudes for the partonic process $gg \to Z\gamma$ and analyze the corresponding angular distributions as well as spin correlations in Z boson decay, and discuss the possible interest of measurements of the Z spin and angular correlations. Our conclusions can be found in section 7.

2 Dimension-8 gluonic QGC operators

Although there are many possibilities for new physics at higher scales above the EW one, the low energy effective field theory (EFT) should be subject to the SM $\mathrm{SU}(3)_c \times \mathrm{SU}(2)_L \times \mathrm{U}(1)_Y$ gauge symmetries. A convenient way to take these symmetries into account is the SMEFT [23], which includes systematically all the allowed interactions with mass dimension $d > 4$. The extra dimensions are compensated by inverse powers of a mass scale M that is associated with heavy new physics. The gQGC operators appear at dimension-8 level with $1/M^4$ suppression [7],

$$\mathcal{O}_{gT,0} \equiv \frac{1}{16M_0^4} \sum_a G^a_{\mu\nu} G^{a,\mu\nu} \times \sum_i W^i_{\alpha\beta} W^{i,\alpha\beta} \,, \tag{2.1a}$$

$$\mathcal{O}_{gT,1} \equiv \frac{1}{16M_1^4} \sum_a G^a_{\alpha\nu} G^{a,\mu\beta} \times \sum_i W^i_{\mu\beta} W^{i,\alpha\nu} \,, \tag{2.1b}$$

$$\mathcal{O}_{gT,2} \equiv \frac{1}{16M_2^4} \sum_a G^a_{\alpha\mu} G^{a,\mu\beta} \times \sum_i W^i_{\nu\beta} W^{i,\alpha\nu} \,, \tag{2.1c}$$

$$\mathcal{O}_{gT,3} \equiv \frac{1}{16M_3^4} \sum_a G^a_{\alpha\mu} G^a_{\beta\nu} \times \sum_i W^{i,\mu\beta} W^{i,\nu\alpha} \,, \tag{2.1d}$$

$$\mathcal{O}_{gT,4} \equiv \frac{1}{16M_4^4} \sum_a G^a_{\mu\nu} G^{a,\mu\nu} \times B_{\alpha\beta} B^{\alpha\beta} \,, \tag{2.1e}$$

$$\mathcal{O}_{gT,5} \equiv \frac{1}{16M_5^4} \sum_a G^a_{\alpha\nu} G^{a,\mu\beta} \times B_{\mu\beta} B^{\alpha\nu} \,, \tag{2.1f}$$

$$\mathcal{O}_{gT,6} \equiv \frac{1}{16M_6^4} \sum_a G^a_{\alpha\mu} G^{a,\mu\beta} \times B_{\nu\beta} B^{\alpha\nu} \,, \tag{2.1g}$$

$$\mathcal{O}_{gT,7} \equiv \frac{1}{16M_7^4} \sum_a G^a_{\alpha\mu} G^a_{\beta\nu} \times B^{\mu\beta} B^{\nu\alpha} \,. \tag{2.1h}$$

In order to respect the SM gauge symmetries, the gauge bosons should appear via their field strengths, such as $G^a_{\mu\nu}$ for gluons together with $W^i_{\mu\nu}$ and $B_{\mu\nu}$ for EW gauge bosons. Since gluons carry QCD color, denoted by the a superscript of $G^a_{\mu\nu}$, the gQGC operators must contain an even number of gluon field strengths, such as $G^a_{\mu\nu} G^{a,\alpha\beta}$, so as to be colorless. The same thing applies for the $\mathrm{SU}(2)_L \times \mathrm{U}(1)_Y$ gauge boson field strengths, for example $W^i_{\mu\nu} W^{i,\alpha\beta}$ and $B_{\mu\nu} B^{\alpha\beta}$. Another symmetry to be imposed is Lorentz invariance. There are four different Lorentz-invariant contractions, as shown above. Hence we must consider eight gQGC operators in total.

JHEP04(2022)123

The total and differential cross sections are largely determined by the Lorentz structure of the gQGC operators. The eight operators can be classified into four pairs $\{\mathcal{O}_{gT,(0,4)}, \mathcal{O}_{gT,(1,5)}, \mathcal{O}_{gT,(2,6)}, \mathcal{O}_{gT,(3,7)}\}$, each with a same Lorentz structure. The W^i and B fields do not correspond to the physical mass eigenstates, which are the photon A and Z boson fields, $W^3 = c_w Z + s_w A$ and $B = c_w A - s_w Z$ where $(c_w, s_w) \equiv (\cos\theta_W, \sin\theta_W)$ are the cosine and sine functions of the weak mixing angle θ_W. Each pair W^iW^i and BB contains AA, AZ and ZZ contributions with coefficients determined by θ_W:

$$\sum_i W^iW^i = W^3W^3 + \cdots = s_w^2 AA + 2c_w s_w ZA + c_w^2 ZZ + \cdots , \tag{2.2a}$$

$$BB = c_w^2 AA - 2c_w s_w ZA + s_w^2 ZZ . \tag{2.2b}$$

We see that their contributions to $gg \to Z\gamma$ scattering via the ZA combination differ only by a sign. Consequently, they produce exactly the same event distributions, and therefore yield identical cross sections for common values of the dimension-8 cut-off scale.

Only 4 independent operators contribute to $gg \to Z\gamma$. On the other hand, in the case of $gg \to \gamma\gamma$, one needs to study separately the 8 operators, as done in [7], and the contributions of BB operators are larger than those of their $\sum_i W^iW^i$ counterparts by a factor $\cot^4\theta_W$. Thus the $\gamma\gamma$ and $Z\gamma$ channels in gluon-gluon scattering are complementary, and their combination can help to disentangle the W^iW^i and BB components within each pair.

For comparison, the Born-Infeld extension of the SM shown in eq. (1.1) contains only one linear combination of the eight gQGC operators,

$$\mathcal{O}_{\rm BISM} \ni \frac{1}{16M_{BI}^4}\left[\mathrm{Tr}(GG)\mathrm{Tr}(WW) + \mathrm{Tr}(G\widetilde{G})\mathrm{Tr}(W\widetilde{W})\right] + \{W \to B\} , \tag{2.3}$$

where the traces are over the Lorentz and SM gauge group indices. The first term involves only CP-even pairs GG and WW of gluon and EW field strengths while the second is composed of the CP-odd combinations $G\widetilde{G}$ and $W\widetilde{W}$. The combinations of CP-odd operators can be rewritten in the form of eq. (2.1), as follows:

$$\mathrm{Tr}(G\widetilde{G})\mathrm{Tr}(W\widetilde{W}) = 4\mathrm{Tr}(GWGW) - 2\mathrm{Tr}(GW)\mathrm{Tr}(GW), \tag{2.4}$$

and similarly for $\mathrm{Tr}(G\widetilde{G})\mathrm{Tr}(B\widetilde{B})$. Hence the BISM contribution to gQGC is simply a linear combination of six gQGC operators in the basis considered above, namely

$$\mathcal{O}_{\rm BISM} \ \ni \ \mathcal{O}_{gT,0} - 2\mathcal{O}_{gT,1} + 4\mathcal{O}_{gT,3} + \mathcal{O}_{gT,4} - 2\mathcal{O}_{gT,5} + 4\mathcal{O}_{gT,7}. \tag{2.5}$$

Most importantly, these six operators share a common cut-off scale M and their coefficients are fully correlated.

It is important to observe that, since the different gauge sectors appear with equal coefficients in the Born-Infeld lagrangian eq. (1.1), the dimension-8 couplings of the EW gauge bosons to gluons take the diagonal form $\sum_i W^iW^i + BB$. Hence, because of the opposite signs and equal magnitudes of the ZA terms in eq. (2.2), the BI extension of the SM does not contribute to $Z\gamma$ production, but only to $\gamma\gamma$ and ZZ production. As we shall see in section 4, the sensitivity to the scale of the BI extension of the SM at the LHC via $gg \to \gamma\gamma$ scattering is considerably greater than that obtained from the study of $\gamma\gamma \to \gamma\gamma$ scattering.

JHEP04(2022)123

3 Properties of the $gg \to Z\gamma$ and $\gamma\gamma$ cross sections

As discussed in section 2, dimension-8 contributions to gluon-gluon collisions can yield $\gamma\gamma$ and $Z\gamma$ final states. Both can provide a clean signal for probing gQGC operators, whilst the BISM can be probed only by the $\gamma\gamma$ channel. This section summarizes the properties of the total and differential $gg \to Z\gamma$ and $\gamma\gamma$ cross sections, discussing the basic features and laying the basis for the analysis of the various Z decay modes in section 4.

3.1 Total cross section and energy dependence

When regarded as a probe of new physics beyond the SM, the sensitivity of the search for a gQGC signal is limited by the possible event rates. A conservative search strategy starts by using the total cross section. Since each gauge field strength ($G^a_{\mu\nu}$, $W^i_{\mu\nu}$, and $B_{\mu\nu}$) contains one derivative and hence contributes one factor of momentum p to the scattering process, the four field strengths in a dimension-8 operator yield a scattering amplitude $\mathcal{M}$ with a p^4 dependence. Taking into account the flux prefactor that is $\propto 1/\hat{s}$ for high-energy scattering, we find that the cross sections given by the gQGC operators grow as $\hat{s}^3 \sim p^6$. Hence the signal cross sections generated by the $\mathcal{O}_{gT,i}$ operators are rapidly-rising functions of the center-of-mass energy $\hat{s}$ of the gluon pair:

$$\sigma_{Z\gamma,i} = \frac{s_w c_w \hat{s}^3 (1-x_Z)^3}{2048\,\pi\, M_i^8} \times \begin{cases} 1 & i = 0, 4, \\ \dfrac{1}{120}\left[13 + 4x_Z + 3x_Z^2\right] & i = 1, 5, \\ \dfrac{1}{480}\left[36 + 3x_Z + x_Z^2\right] & i = 2, 6, \\ \dfrac{1}{480}\left[23 + 4x_Z + 3x_Z^2\right] & i = 3, 7, \end{cases} \tag{3.1}$$

where $x_Z \equiv m_Z^2/\hat{s}$. This effect enhances the signal event rate significantly at higher energy, as shown in figure 1, where we see that the signal grows very fast whereas the SM background decreases $\propto 1/\sqrt{\hat{s}}$. Thus one expects to find greater sensitivities at higher-energy colliders, as we discuss later.

The steadily growing cross sections finally violate the unitarity bound at some center-of-mass energy scale [7]. This problem can be addressed by introducing momentum-dependent couplings or unitarization procedures [24], or by estimating the maximum center-of-mass energy allowed by unitarity [25]. Following the procedure adopted in [6] and [7], here we respect the unitarity constraint by assuming that the cross section falls as $\hat{s}^{-1}$ once the "tree unitarity" requirement [26] is satisfied, after which the energy scaling is the same as that of the major irreducible background due to $\bar{q}q \to \gamma\gamma$. We find that this unitarity bound $\sigma \sim 1/m^2_{Z\gamma}$ is saturated at the gluon-gluon center-of-mass energies

$$\sqrt{\hat{s}_i} = M_i \left[\frac{s_w c_w}{2048\,\pi}\left(1, \frac{13}{120}, \frac{36}{480}, \frac{23}{480}\right)\right]^{-1/8}, \tag{3.2}$$

for $i = (0,4), (1,5), (2,6), (3,7)$, in the limit $x_Z \to 0$. For $\hat{s} = 1\,\text{TeV}^2$, the ratio $x_Z \lesssim 0.01$ is generally negligible.

JHEP04(2022)123

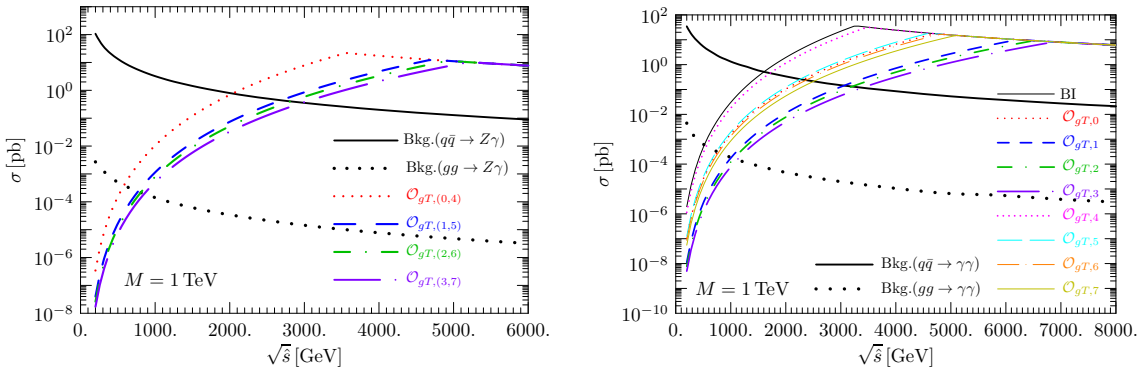

Figure 1. The total cross sections for $gg \to Z\gamma$ (left) and $gg \to \gamma\gamma$ (right) generated by the different dimension-8 gQGC operators at the parton level (colorful non-solid lines). For illustration, we assume that the scattering amplitudes have equal cut-off scales $M = 1\,\text{TeV}$ until their respective cross sections reach their unitarity limits, which we assume to be saturated at higher gluon-gluon centre-of-mass energies $\sqrt{\hat{s}}$. The cross sections for the SM background from $q\bar{q}$ annihilation are shown as solid black lines.

The sensitivity to the scale of new physics is quite stable with respect to the choice of unitarization scheme. For example, an aggressive unitarization scheme that cuts off the signal events above the saturation point would reduce the total event rate by a factor of about 2. But the dependence on the new physics scale M_i is eighth power, $\sigma \propto 1/M_i^8$, so the sensitivity is reduced by only 10% at most. In following discussions, the same unitarization scheme $\sigma \sim 1/\hat{s}$ is applied for both the current LHC-13 TeV with real data and the future experiments with projected pseudo-data.

The total cross sections for $gg \to Z\gamma$ and $\gamma\gamma$ are summarized in figure 1 as functions of $\sqrt{\hat{s}}$, with $M_i = 1\,\text{TeV}$ for illustration. The signal cross sections are much larger than the SM background for $\sqrt{\hat{s}} \gtrsim 2\,\text{TeV}$, and the tree unitarity limits are reached when $\sqrt{\hat{s}_i} = (3.58, 4.72, 4.94, 5.22)M_i$ for $i = (0,4),(1,5),(2,6),(3,7)$ for the $gg \to Z\gamma$ process; $\sqrt{\hat{s}_i} = (4.71, 6.21, 6.51, 6.88, 3.49, 4.60, 4.82, 5.10)M_i$ for $i = 0, \ldots, 7$ for the $gg \to \gamma\gamma$ process; and $\sqrt{\hat{s}_i} = 3.26M_i$ for the BI model. Even when the unitarity bound is imposed for $gg \to Z\gamma$, replacing its rapidly-growing cross section with the SM $1/\hat{s}$ scaling, the signal is almost two orders above the SM background, as seen in the left panel of figure 1. For comparison, in the case of the cross section for the $\gamma\gamma$ channel shown in the right panel, the difference between signal and background is close to three orders of magnitude. This indicates that the $gg \to Z\gamma$ and $\gamma\gamma$ signals should be readily detectable at high-energy hadron colliders if gQGC operators appear at the TeV scale. Details of a more complete study are given below.

Figure 1 also shows the next-to-leading order (NLO) SM background due to $gg \to Z\gamma$ via box diagram. Its cross section has been calculated using `MadGraph@NLO` [42] to calculate the loop diagram automatically. Due to the loop factor, this gg background is suppressed by roughly four orders of magnitude compared to its $q\bar{q}$ counterpart. In addition to its own contribution, this loop-induced $gg \to Z\gamma$ scattering amplitude can also interfere with the dimension-8 operator amplitude. However, for this interference term to be comparable with the $q\bar{q}$ background, the dimension-8 operator amplitude would need to be two orders larger

JHEP04(2022)123

than the $q\bar{q}$ one. In this case, the signal is much stronger than background. In the case that the signal is comparable with the background, i.e., the dimension-8 operator contribution is comparable with the $q\bar{q}$ one, the interference term is two orders smaller. In either case, the loop-induced SM gg background is negligible. Hence, in the following discussion we focus on the SM $q\bar{q}$ background and the $gg \to Z\gamma$ signal.

We note that dimension-6 operators could in principle contribute to the same final state $pp \to Z\gamma$. It could well be that such operators are absent, but their presence would not invalidate our analysis. We recall that the amplitude for a $2 \to 2$ process is dimensionless. With a coefficient that is $\propto 1/\Lambda^2$, where Λ is the corresponding new-physics scale, the contribution to the amplitude should scale as s/Λ^2 due to dimensional analysis. Comparing with the dimension-8 contribution that scales with s^2/Λ^4, the dimension-6 operator is suppressed in the high-energy signal region $\sqrt{\hat{s}} \gtrsim 1\,\text{TeV}$. Hence dimension-6 operators are not a problem for our study of the collider sensitivities to dimension-8 gQGC operators in this paper. We note that this argument based on dimensional analysis applies to any dimension-6 operator, and is independent of its concrete form.

3.2 Angular distribution and background suppression

The SM background mainly comes from t-channel $q\bar{q} \to Z\gamma$ scattering. This process is intrinsically suppressed at large angles by the intermediator quark propagator, which is $\propto 1/\hat{t}$ in the massless limit. For a fixed ratio between the Mandelstam variables $\hat{s}$ and $\hat{t}$, the leading-order cross section for the SM background is given by

$$\sigma_{q\bar{q}\to Z\gamma} = \frac{Q_q^4 g_E^4}{24\pi\hat{s}} \left[\frac{(T_3^q)^2}{Q_q^2 s_w^2 c_w^2} - \frac{2T_3^q}{Q_q c_w^2} + 2\frac{s_w^2}{c_w^2}\right] \left[\frac{2(1+x_Z^2)}{1-x_Z}\left[\tanh^{-1}(1-\delta) - 1 + \delta\right] - \frac{1}{3}(1-x_Z)\right], \tag{3.3}$$

where $\delta \sim 0$ is an infrared regulator that scales as $1/\hat{s}$ in the high-energy limit. The ratio between the quark mass m_q and $m_{Z\gamma}$, $m_q/m_{Z\gamma}$, would in principle provide a natural cut-off value for the scattering angle, but in practice $m_q/m_{Z\gamma}$ is much smaller than typical kinematic cuts for event selection, and hence is irrelevant for our purposes. Although the SM background decreases as $1/\hat{s}$, it will still dominate the event rate if the cut-off scales M_i of the gQGC operators are much higher than the 1 TeV used in figure 1. For this reason, it is desirable to find kinematic cuts to suppress the SM background.

One such cut-off is provided by the scattering angle in the center-of-mass frame [7], since the Z and photon are emitted as initial state radiation in the t-channel exchange process and hence are typically quite forward. The differential cross section $d\sigma/d\cos\vartheta$ [27] is

$$\frac{d\sigma_{q\bar{q}\to Z\gamma}}{d\cos\vartheta} = \frac{Q_q^4 e^4}{24\pi\hat{s}} \left[\frac{(T_3^q)^2}{Q_q^2 s_w^2 c_w^2} - \frac{2T_3^q}{Q_q c_w^2} + 2\frac{s_w^2}{c_w^2}\right] \left[\frac{1+x_Z^2}{1-x_Z} - \frac{1}{2}(1-x_Z)\sin^2\vartheta\right] \cot^2\vartheta, \tag{3.4}$$

where T_3^q and $Q_q e$ are the quark isospin and electric charges. As shown by the black curve in figure 2, the SM background indeed peaks in the forward and backward directions, where $\cos\vartheta = \pm 1$. The comparison between the left panel ($\sqrt{\hat{s}} = 100\,\text{GeV}$) and the right panel ($\sqrt{\hat{s}} = 1\,\text{TeV}$) shows that higher energy leads to more forward scattering. This property applies to both the $Z\gamma$ and $\gamma\gamma$ channels.

JHEP04(2022)123

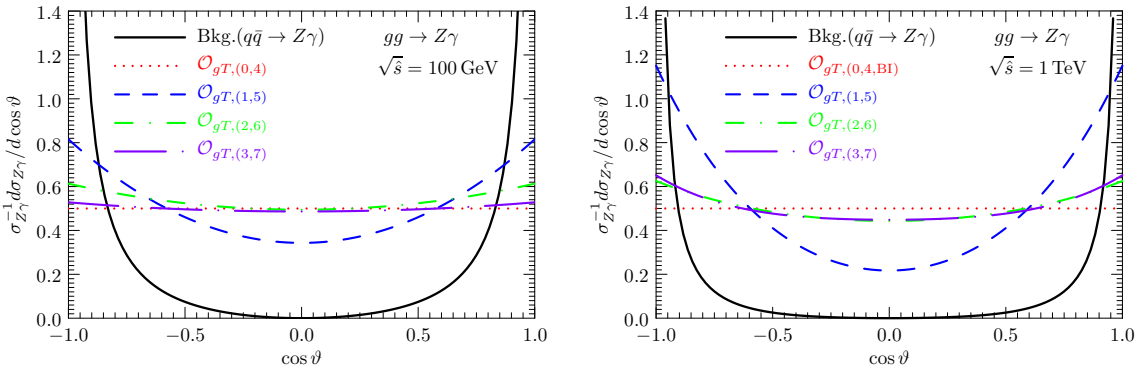

Figure 2. Distributions in the normalized scattering angle $\cos\vartheta$ for $gg \to Z\gamma$ scattering from the gQGC operators (colorful non-solid curves) and the SM background $q\bar{q} \to Z\gamma$ (black solid curve). The energy dependences are seen by comparing the left ($\sqrt{\hat{s}} = 100\,\text{GeV}$) and right ($\sqrt{\hat{s}} = 1\,\text{TeV}$) panels.

For comparison, the signal distribution is much less forward-backward peaked than the SM background. The differential cross sections for the $gg \to Z\gamma$ process generated by the dimension-8 operators are

$$\frac{d\sigma_{gg\to Z\gamma}}{d\cos\vartheta} = \frac{s_w c_w (1-x_Z)^3 \hat{s}^3}{4096\pi M_i^8} \times \begin{cases} 1 & i = 0,4\,, \\ \frac{1}{512}\Big[73+52\cos(2\vartheta)+3\cos(4\vartheta)+24x_Z^2\sin^4(\vartheta) & \\ \qquad +8x_Z\sin^2\vartheta\big(5+3\cos(2\vartheta)\big)\Big] & i = 1,5\,, \\ \frac{1}{2048}\Big[163+28\cos(2\vartheta)+\cos(4\vartheta)+8x_Z^2\sin^4\vartheta & \\ \qquad +8x_Z\sin^2\vartheta\big(3+\cos(2\vartheta)\big)\Big] & i = 2,6\,, \\ \frac{1}{2048}\Big[105+20\cos(2\vartheta)+3\cos(4\vartheta)+24x_Z^2\sin^4\vartheta & \\ \qquad +8x_Z\sin^2\vartheta\big(5+3\cos(2\vartheta)\big)\Big] & i = 3,7\,. \end{cases} \tag{3.5}$$

These angular distributions are the same as for the $gg \to \gamma\gamma$ case [7] in the limit $x_Z \to 0$, reflecting the fact the limit $x_Z \to 0$ corresponds to a massless Z boson that is no different from a massless photon. Since the Z boson mass is significantly smaller than the typical invariant mass $m_{Z\gamma}$ at hadron colliders, the correction due to a finite x_Z is generally negligible.

The differences between the gQGC signals (colorful non-solid lines) and the SM background (black solid line) in figure 2 are prominent. Since the polarizations of the incoming gluons are unknown, the process is symmetric under the interchange $g(\vec{p}_1) \leftrightarrow g(\vec{p}_2)$. This means that there is a symmetry in the polar angle under $\vartheta \to \pi - \vartheta$, under which $\sin\vartheta \to \sin\vartheta$ and $\cos\vartheta \to -\cos\vartheta$. Figure 2 shows that $\mathcal{O}_{gT,(0,4)}$ yield isotropic distributions, whereas the other gQGC operators yield distributions that have small forward-backward peaks. The four Lorentz structures have quite different distributions in general, but we note the following similarities. At the low energy $\sqrt{\hat{s}} = 100\,\text{GeV}$ in the left panel, $\mathcal{O}_{gT,(0,4)}$ and

JHEP04(2022)123

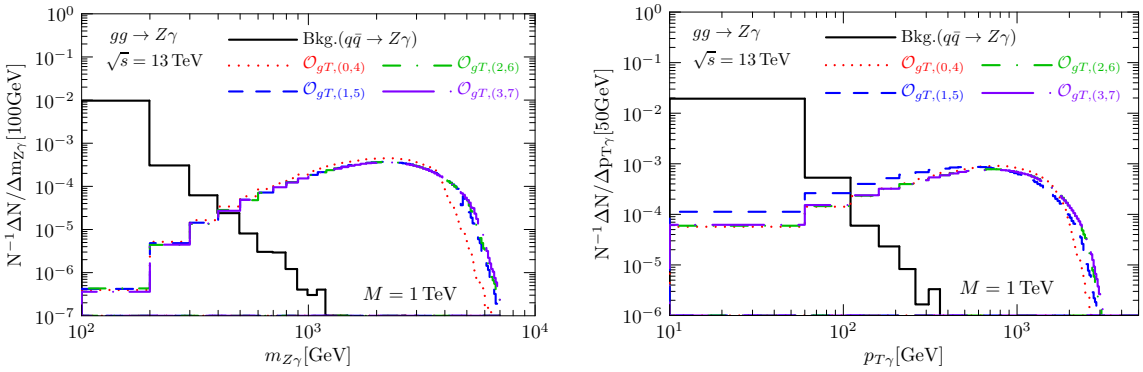

Figure 3. The normalized event spectra due to the background (black solid line) and gQGC operators (colorful non-solid lines) as functions of the $Z\gamma$ invariant mass $m_{Z\gamma}$ (left) and the photon transverse momentum $p_{T\gamma}$ (right) at the LHC with $\sqrt{s} = 13\,\text{TeV}$. As seen more clearly in the left panel, the total cross sections have been regulated to respect the unitarity constraint.

$\mathcal{O}_{gT,(3,7)}$ yield similar angular distributions, whereas in the right panel at $\sqrt{\hat{s}} = 1\,\text{TeV}$ there is greater similarity between the angular distributions for $\mathcal{O}_{gT,(2,6)}$ and $\mathcal{O}_{gT,(3,7)}$.

Since the gQGC signals have only mild anisotropies, whereas the SM background is concentrated in the forward and backward regions, a simple cut on the Z/γ polar scattering angle in the rest frame of the gg system can suppress significantly the SM background and thereby enhance the signal sensitivity. This feature is used in our study of the experimental sensitivities at the LHC and future colliders in section 4. The potential for distinguishing different gQGC operators via the angular distributions is discussed further in section 6.

4 Search strategy and sensitivities at hadron colliders

As discussed above, probes of the gQGC operators at hadron colliders with the processes $gg \to Z\gamma$ and $\gamma\gamma$ are potentially interesting. The signals would dominate over the SM background when the gg center-of-mass energy reaches the TeV scale, and a simple cut on the scattering angle can further enhance the sensitivity significantly. In this section, we study more details of possible experimental probes. The photon signal at a hadron collider is very clear, so we simply use photon information to obtain sensitivities for the $gg \to \gamma\gamma$ channel. The event spectrum for the $gg \to \gamma\gamma$ process has been studied carefully in [7], and we discuss the updated sensitivity of $gg \to \gamma\gamma$ in section 4.1.

The normalized event spectra for $gg \to Z\gamma$ due to the various dimension-8 operators at the LHC with $\sqrt{s} = 13\,\text{TeV}$ are shown in figure 3. The major differences between figure 1 and figure 3 are due to the gluon parton distribution function (PDF) in proton, which suppresses the high-energy tails of the event spectra. This makes the difference between the gQGC signals and the SM background even more prominent, and reduces the sensitivity to the treatment of the unitarity constraint. Spectra in the $Z\gamma$ invariant mass $m_{Z\gamma}$ are shown in the left panel of figure 3 and the photon transverse momentum $p_{T\gamma}$ distributions are shown in the right panel.[1] Comparing the two panels of figure 3, we see that the $p_{T\gamma}$

[1] Analogous $m_{\gamma\gamma}$ distributions for $gg \to \gamma\gamma$ scattering were shown in figure 2 of [7].

JHEP04(2022)123

spectra grow more slowly. In the cases of charged-fermion final states, $Z \to \ell^+\ell^-$ and $q\bar{q}$, the invariant mass spectrum contains more information, by virtue of the $p^8 \sim s^4$ energy dependence. However, in the case of the decays into neutrinos, $Z \to \nu\bar{\nu}$, the only reliable experimental information is provided by the photon transverse momentum $p_{T\gamma}$.

We study individually the Z boson decays into various fermion-antifermion pairs: decays into charged leptons, $Z \to \ell^+\ell^-$, in section 4.2; decays into neutrinos, $Z \to \bar{\nu}\nu$, in section 4.3; and decays into quarks, $Z \to q\bar{q}$, in section 4.4. The prospects for all these channels at the future hadron colliders (HE-LHC, FCC-hh, and SppC) are studied in section 5. The event rates in this paper are simulated with `MadGraph5` [28] with model files prepared by `Feynrules` [29] in the UFO format [30] for the leading order (LO) results. NLO corrections to the background at $\sqrt{s} = 13$ TeV are taken into account by an overall K-factor that is extracted by comparing our LO calculations with the NLO calculations given in the experimental papers (the $pp \to \gamma\gamma$ process reported in [33], the $pp \to Z\gamma$ processes in [20] for the leptonic channel and [21] for the invisible decay channel as well as [22] for the hadronic channel). For future colliders, we have used the same overall K-factor.

We adopt the same binning for the prospective signals, $N_i^{\rm sig}$, as has been used for the corresponding experimental data points, $N_i^{\rm data}$. On the basis of these numbers, we use the following χ^2 function to evaluate the sensitivity to the dimension-8 gQGC operators:

$$\chi^2 = \sum_i \left[\frac{N_i^{\rm data} - F N_i^{\rm bkg} \Pi_k (1 + \bar{\sigma}_{k,i} + f_k \sigma_{k,i}) - N_i^{\rm sig}}{\sqrt{N_i^{\rm data}}} \right]^2 + \sum_k f_k^2 . \tag{4.1}$$

In addition to the cut-off scale M_i that enters implicitly through the signal event rates $N^{\rm sig}(M_i)$, the χ^2 function also contains an overall normalization F and multiple nuisance parameters f_k to account for the various systematics published in the experimental papers. For each systematical error, both the central value $\bar{\sigma}_i$ and the deviations $f_k\sigma_{k,i}$ have been taken into account. Assuming quadratic dependences on the nuisance parameters F and f_k, the χ^2 minimization can be done analytically [31, 32]. After marginalizing over F and f_k, the resulting $\chi^2(M_i)$ as function of a single parameter provides the sensitivity to the cut-off scale M_i. The same procedure has been followed for the SM background, so as to calculate $\chi^2_{\rm min}$. The square root of the difference, $\Delta\chi^2(M_i) \equiv \chi^2(M_i) - \chi^2_{\rm min}$, directly gives the significance that we show below. We generally quote results at the 95% C.L., corresponding to $\Delta\chi^2 = 3.84$. The sensitivities shown in this paper are obtained for each of the 8 gQGC operators separately and for the BISM combination. The constraints on the individual operator coefficients would in general be weaker if all the operators were included simultaneously and one marginalized over the other operator coefficients.

Below we apply this χ^2 analysis to the ATLAS data for various channels. To guarantee that the quadratic χ^2 function is a good enough approximation, only those bins with at least 5 events are included in eq. (4.1). This provides a very conservative sensitivity estimation, since beyond the end points of the SM background (or the experimental data), the signal is still growing and essentially free of background. If a more sophisticated data analysis were employed, the sensitivity could be further improved. We leave this to our experimental colleagues.

JHEP04(2022)123

4.1 $pp \to \gamma\gamma$ at the LHC

We first update the analysis of [7] using the ATLAS measurement of the diphoton invariant mass $m_{\gamma\gamma}$ spectrum using $36.7\,\text{fb}^{-1}$ to include $139\,\text{fb}^{-1}$ [33], which provides improved sensitivities to dimension-8 operators. The left panel of figure 4 displays the updated results from analyzing the ATLAS data on isolated $\gamma\gamma$ production. Because of the different electroweak mixing angle factors in eq. (2.2), the $\sum_i W^i W^i$ operators $\mathcal{O}_{gT,(0,1,2,3)}$ with coefficients s_w^2 are constrained more weakly than their BB counterparts $\mathcal{O}_{gT,(4,5,6,7)}$, which have factors c_w^2 instead. The 95% C.L. lower limits on the mass scales M_i reach $\simeq 1.3\,\text{TeV}$ for $\mathcal{O}_{gT,(1,2,3)}$, $\simeq 1.8\,\text{TeV}$ for $\mathcal{O}_{gT,(0,5,6,7)}$, and $\simeq 2.5\,\text{TeV}$ for $\mathcal{O}_{gT,4}$. Since the improvement comes principally from the updated luminosity, further enhancement in the collision energy and luminosity at the LHC can push the limits to higher values. The right panel of figure 4 shows the prospects for LHC running at the design energy $\sqrt{s} = 14\,\text{TeV}$ with integrated luminosity $\mathcal{L} = 3\,\text{ab}^{-1}$ [34]. The constraints at the same 95% C.L. can improve by amounts ~ 1 to $2\,\text{TeV}$.

The solid black line in figure 4 represents the sensitivity to the Born-Infeld $\mathcal{O}_{gT,BI}$ combination of the gQGC operators in eq. (2.5). This linear combination of 6 individual gQGC operators yields an event rate that is much larger than any individual operator, as seen in figure 1. Consequently, the 95% CL lower limit on the BISM mass scale reaches $M_{BI} \gtrsim 5\,\text{TeV}$. This result is strong enough to impose a significant constraint on the separation between branes in some M-theory inspired models that address the electroweak hierarchy problem.

We emphasize that we are working to quadratic order in the dimension-8 operator coefficients, unlike many analyses of dimension-6 operators at the LHC. Also, our analysis is reliant on values of $\sqrt{\hat{s}}$ that are below those where the unitarity constraints become important. However, we also note that in some instances the values of $\sqrt{\hat{s}}$ contributing to our analysis are comparable to (or even exceed) the magnitudes of the constraints on new-physics scale M_i that we derive. In such cases, the validity of our constraints depends on the magnitude of the new-physics coupling. They would be most reliable if the dimension-8 operator were generated by some strongly-coupled new physics at a scale Λ with coupling strength 4π, in which case $\Lambda = \sqrt{4\pi}M$ would generally exceed the values of $\sqrt{\hat{s}}$ that provide the constraints in our analysis.

The CMS and TOTEM collaborations have recently searched for exclusive diphoton production in proton-proton collisions and set constraints on the dimension-8 quartic photon couplings $\zeta_1 F_{\mu\nu}F^{\mu\nu}F_{\rho\sigma}F^{\rho\sigma}$ and $\zeta_2 F_{\mu\nu}F^{\mu\rho}F_{\rho\sigma}F^{\sigma\nu}$ [18]. Their result is a two-dimensional contour in the plane of the coefficients ζ_1 and ζ_2, in the absence of theoretical constraints. As demonstrated earlier, the Born-Infeld QED extension in eq. (1.1) naturally correlates the two purely photon QGC operators with $\zeta_1 = \zeta_2 = 1/32M^4$. Thus the 95% sensitivity of the CMS-TOTEM data becomes $M_{\text{BI}} \geq 670\,\text{GeV}$. The CMS and TOTEM sensitivity is limited by the fact that it uses $\gamma\gamma \to \gamma\gamma$ scattering with photons in both the initial and final states, leading to a weaker constraint than the $gg \to \gamma\gamma$ process at the same collider for either individual operator or the combined BISM operator. This confirms the advantage of considering the $gg \to \gamma\gamma$ channel at hadron colliders.

JHEP04(2022)123

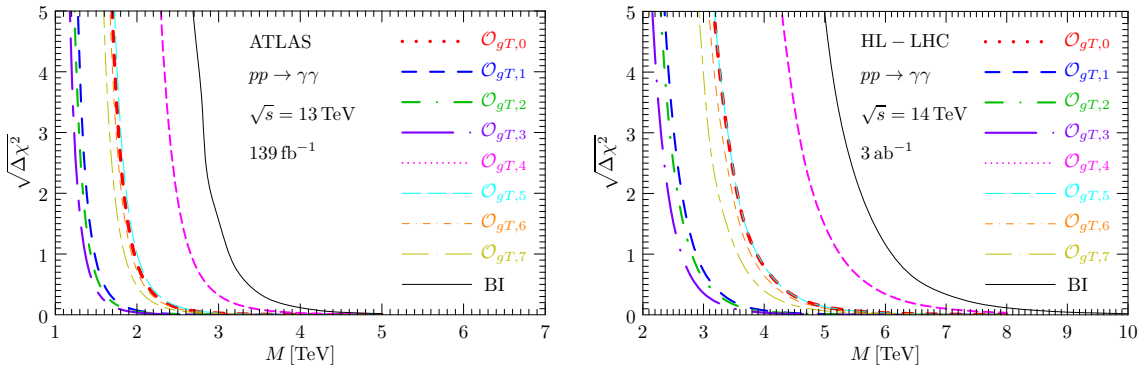

Figure 4. The significances $\sqrt{\Delta\chi^2}$ for probes of the individual dimension-8 gQGC operators $\mathcal{O}_{gT,i}$ and their Born-Infeld combination in eq. (2.5) at the LHC as functions of the cut-off scales M_i. These results are obtained from the $gg \to \gamma\gamma$ reaction at $\sqrt{s} = 13\,\text{TeV}$ with integrated luminosity $\mathcal{L} = 139\,\text{fb}^{-1}$ observed by ATLAS (left) and $\sqrt{s} = 14\,\text{TeV}$ with $\mathcal{L} = 3\,\text{ab}^{-1}$ at HL-LHC (right).

4.2 $pp \to Z(\ell^+\ell^-)\gamma$ at the LHC

The ATLAS Collaboration has searched for new physics in the $Z(\ell^+\ell^-)\gamma$ final state with an integrated luminosity of $139\,\text{fb}^{-1}$ [20] at $\sqrt{s} = 13$ TeV. Here we re-interpret the results with electron ($Z \to e^+e^-$) and muon ($Z \to \mu^+\mu^-$) final states as constraints on the gQGC operators. Both the photon and the charged leptons are observable. The event selection required the photon to have pseudo-rapidity in the range $|\eta^\gamma| < 2.37$ and transverse energies $E_T^\gamma > 30\,\text{GeV}$. We use the ATLAS data with tight photon identification, which had an identification efficiency ranging from 82−85% for $E_T^\gamma \approx 30\,\text{GeV}$ to 90–98% for $E_T^\gamma > 100\,\text{GeV}$. The electrons and muons are required to have pseudo-rapidities $|\eta^\ell| < 2.47$ and transverse momenta $p_T^\ell > 25\,\text{GeV}$. The identification efficiency for charged leptons is about 80% (93%) for $p_T \approx 25\,\text{GeV}$ (100 GeV). Because of geometrical limitations, the transition region between the barrel and endcap ($1.37 < |\eta| < 1.52$) is excluded for both the photon and the charged leptons.

The dominant instrumental backgrounds for the $Z(\ell^+\ell^-)\gamma$ final states are Z + jets, pile-up events with one photon, $t\bar{t}\gamma$ and $\tau^+\tau^-\gamma$, as well as double vector boson production with or without an isolated photon [20]. It was estimated that the combination of these backgrounds contributes about 18% of the signal process $q\bar{q} \to Z(\ell^+\ell^-)\gamma$ in the fiducial phase space. For simplicity, we take the `Sherpa` simulation of the background from the ATLAS paper [20] and assign an overall normalization factor F when fitting the experimental data as explained in the discussion of eq. (4.1).

The left panel of figure 5 shows the sensitivities obtained from fitting the observed $Z(\to \ell^+\ell^-)\gamma$ invariant mass $m_{Z\gamma}$ spectrum at ATLAS [20] for probing the gQGC operators. Since the contributions of $GG\sum_i W^iW^i$ and $GGBB$ operators with the same Lorentz structures have identical EW mixing factors for the $Z\gamma$ combination, except for a relative sign, see eq. (2.2), the sensitivities to $\mathcal{O}_{gT,i}$ and $\mathcal{O}_{gT,i+4}$ (i = 0, 1, 2, 3) are pairwise identical. Hence we plot only 4 curves, for $\mathcal{O}_{gT,(0,4)}$ (red), $\mathcal{O}_{gT,(1,5)}$ (blue), $\mathcal{O}_{gT,(2,6)}$ (black), and $\mathcal{O}_{gT,(3,7)}$ (green), respectively. The 95% C.L. lower limits on the new physics scales M_i

JHEP04(2022)123

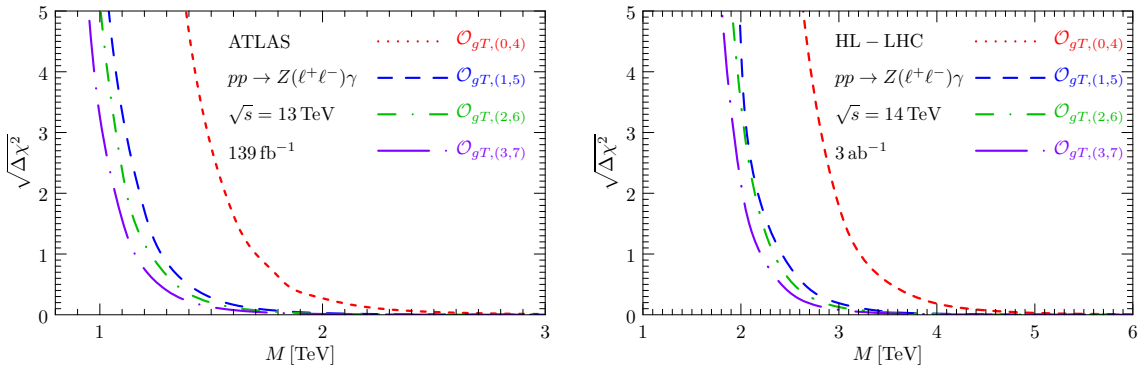

Figure 5. The significances $\sqrt{\Delta\chi^2}$ for probes of the individual dimension-8 gQGC operators $\mathcal{O}_{gT,(i,i+4)}$, where $i = 0, 1, 2, 3$, from the $Z(\ell^+\ell^-)\gamma$ channel as functions of the cut-off scales M_i. The left panel shows the sensitivities obtained using the current LHC data with $\sqrt{s} = 13\,\text{TeV}$ and luminosity $\mathcal{L} = 139\,\text{fb}^{-1}$, and the right panel shows the estimated sensitivities for the future HL-LHC with $\sqrt{s} = 14\,\text{TeV}$ and $\mathcal{L} = 3\,\text{ab}^{-1}$.

can reach $\simeq 1\,\text{TeV}$ for $\mathcal{O}_{gT,(1,2,3,5,6,7)}$ and $\simeq 1.7\,\text{TeV}$ for $\mathcal{O}_{gT,(0,4)}$. For comparison, the right panel of figure 5 shows the prospects at the HL-LHC with $\sqrt{s} = 14\,\text{TeV}$ and integrated luminosity $\mathcal{L} = 3\,\text{ab}^{-1}$. We see that the lower limits are enhanced by roughly 1 TeV.[2]

With three detectable particles in the final state, much more information can in principle be extracted beyond just the invariant mass, pseudo-rapidity, and transverse momentum. For example, ATLAS also analyzed the angular distribution of the $\ell^+\ell^-$ pair relative to the scattering plane. We discuss in section 6 potential improvements of the cross-section analysis using spin and angular correlation measurements.

4.3 $pp \to Z(\bar{\nu}\nu)\gamma$ at the LHC

The detection of the $Z(\bar{\nu}\nu)\gamma$ final state differs from those of the diphoton channel and the $gg \to Z(\ell^+\ell^-)\gamma$ mode, since only the photon is observable. This renders impossible the reconstruction of the invariant mass spectrum that is the optimal choice for seeing the momentum dependence of the dimension-8 gQGC operators. The only usable information is the photon energy/momentum vector. Although this can readily be measured, the information cannot be fully used since the initial momenta of the colliding gluons in the beam protons are unknown. Because of this uncertainty, one can only utilize the transverse momentum spectrum depicted in the right panel of figure 3. Although not optimal, it still possesses the feature that the event rate keeps growing with momentum until the unitarity saturation is encountered and the gluon PDF suppression finally dominates.

The ATLAS measurement of $Z(\to \bar{\nu}\nu)+\gamma$ uses an integrated luminosity of $\mathcal{L} = 36.1\,\text{fb}^{-1}$ at 13 TeV [21]. The event selection uses the following experimental cut on the transverse energy: E_T^γ, $E_T^{\text{miss}} > 150\,\text{GeV}$. Similarly to the charged lepton case, the photon pseudo-rapidity is in the range $|\eta^\gamma| < 2.37$, but excluding $1.37 < |\eta^\gamma| < 1.52$ to avoid the gap between the detector barrel and end-cap regions. The transverse missing momentum p_T^{miss}

[2]We recall that the $Z\gamma$ final state does not provide any constraint on the Born-Infeld scale, since the contributions of the W^3W^3 and BB operators cancel with each other as explained below eq. (2.2).

JHEP04(2022)123

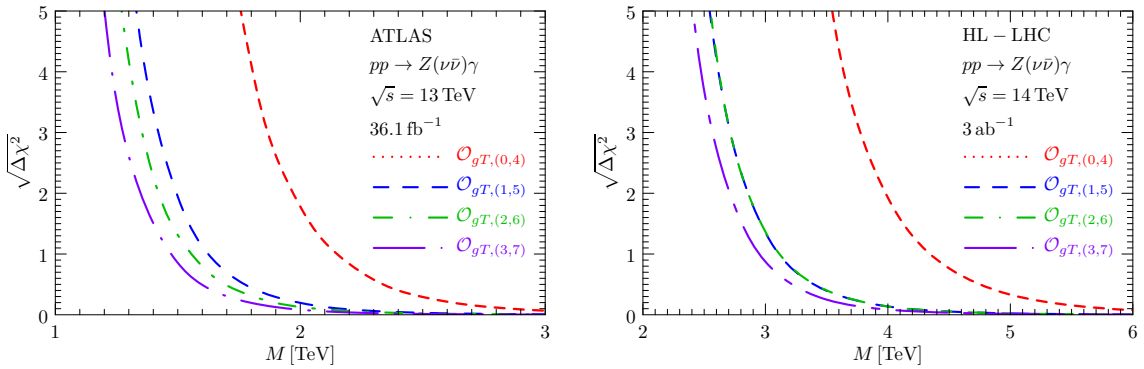

Figure 6. The significances $\sqrt{\Delta\chi^2}$ for probes of the individual dimension-8 gQGC operators $\mathcal{O}_{gT,(i,i+4)}$, where $i = 0, 1, 2, 3$, from the $Z(\nu\bar{\nu})\gamma$ channel as functions of the cut-off scales M_i. The left panel shows the sensitivities obtained using the current LHC data with $\sqrt{s} = 13\,\text{TeV}$ and luminosity $\mathcal{L} = 36.1\,\text{fb}^{-1}$ while the right panel shows the estimated sensitivities for the future HL-LHC with $\sqrt{s} = 14\,\text{TeV}$ and $\mathcal{L} = 3\,\text{ab}^{-1}$.

needs not be opposite to the photon transverse momentum p_T^γ, due to parton shower from the initial gluons. Requiring the azimuthal angular difference $\Delta\phi(p_\gamma, p_T^{\text{miss}}) > \pi/2$ further suppresses the background.

The dominant instrumental background for the $Z(\bar{\nu}\nu)\gamma$ final state comes from $W\gamma$ associated production with the W decaying leptonically but the charged lepton from $W \to \ell\nu$ not being identified. In addition, jets $+\gamma$ and other events with either an electron or a jet being misidentified as a γ are possible sources of background [21]. These backgrounds can amount to about 68 (58)% of the inclusive (exclusive) SM background $q\bar{q} \to Z(\bar{\nu}\nu)\gamma$ in the fiducial phase space, i.e., the cross section with $\geq 0\,(0)$ additional jets.

The sensitivities from analytical χ^2 fits to the different gQGCs obtained using eq. (4.1) are shown in the left panel of figure 6. Although the $pp \to Z(\bar{\nu}\nu)\gamma$ channel is not the optimal one, the lower bound on the cut-off scale M at 95% C.L. can still reach around 1.4 TeV for $\mathcal{O}_{gT,(1,2,3,5,6,7)}$ and 1.9 TeV for $\mathcal{O}_{gT,(0,4)}$. One reason is that the $Z \to \bar{\nu}\nu$ mode includes all three neutrinos whereas only electron and muon modes are used for the charged lepton mode. Moreover, the Z decay branching ratio into a single neutrino is roughly double that of its charged lepton counterpart, so the combined $Z \to \bar{\nu}\nu$ branching ratio is about three times larger than the combined $Z \to \ell^+\ell^-$ branching ratio. The right panel of figure 6 shows the prospects at the HL-LHC with its higher energy and luminosity. The lower bounds are improved by $\gtrsim 1$ TeV.

4.4 $pp \to Z(q\bar{q})\gamma$ at the LHC

The leptonic modes discussed in the previous sections have very clean signals at the hadron colliders. However, although the hadronic decay modes of the Z boson have more complicated backgrounds, the larger branching ratio provides some advantages. The ATLAS Collaboration has measured the $Z(\to \bar{q}q)\gamma$ $m_{Z\gamma}$ invariant mass spectrum with an integrated luminosity of $\mathcal{L} = 36.1\,\text{fb}^{-1}$ at 13 TeV [22]. The experimental analysis first selected events containing a hadronic jet with $p_T > 200\,\text{GeV}$ and $|\eta| < 2.0$ in addition to a photon with

JHEP04(2022)123

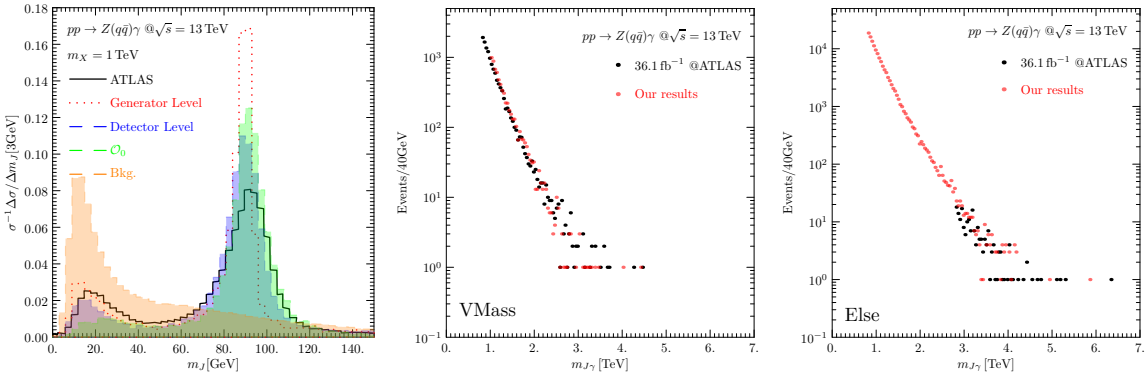

Figure 7. Validations of our simulation of the hadronic decay mode $Z \to q\bar{q}$, assuming a scalar resonance X with mass $m_X = 1\,\text{TeV}$. The left panel shows the invariant mass distribution of a fat jet emerging from the decay of a highly-boosted Z-boson while the middle and right panels compare distributions of the invariant mass $m_{J\gamma}$ for the VMass and Else categories.

$p_T^\gamma > 250\,\text{GeV}$ and $|\eta| < 1.37$. The events were then divided into four categories [22]: 1) The BTAG category of events in which the two leading track-jets associated with a large-radius jet candidate satisfy the jet mass requirement for b-tagging, with a $Z \to \bar{q}q$ identification efficiency of 3 to 4%; 2) The D2 category that is composed of events satisfying combined jet mass and substructure discriminant requirements with an identification efficiency of 20 to 28%; 3) The VMass category containing events that pass the jet mass selection but fail to enter either of the two previous categories (identification efficiency 24 to 36%); and 4) The Else category containing the remaining events that pass the baseline selection (identification efficiency 40 to 50%). Roughly speaking, the event rates in the above four categories increase by an order of magnitude going from category 1) to category 4). Figure 7 shows some validation results from our simulation obtained using `Pythia8` [35] for parton shower effects and `Delphes3` [36] for detector effects, as well as `FastJet`[37], `ExRootAnalysis`[28] and `Root` [38] for data analysis. The invariant mass distribution in the left panel reproduces adequately the Z boson peak and a lower background peak around 20 GeV. Since the event rate is dominated by the VMass and Else categories, we only show these two in the middle and right panels. Our simulations are reasonably consistent with the ATLAS data points.

The sensitivities for the $pp \to Z(q\bar{q})\gamma$ channel at the LHC are shown in figure 8 for both the current LHC data (left panel) and the future HL-LHC (right panel). Although the hadronic modes are much more difficult to detect, the 95% C.L. lower bound still reaches around 1.5 TeV for $\mathcal{O}_{gT,(1,2,3,5,6,7)}$ and 2.3 TeV for $\mathcal{O}_{gT,(0,4)}$, which are even stronger than the neutrino mode. Further improvement by at least another 1 TeV should be possible at HL-LHC. In addition to the pseudo-rapidity and transverse momentum, the angular distribution of the $\bar{q}q$ pair relative to the scattering plane can also be measured. However, this was not done in the ATLAS analysis [22]. A discussion of possible future improvements using this information is given in section 6.

JHEP04(2022)123

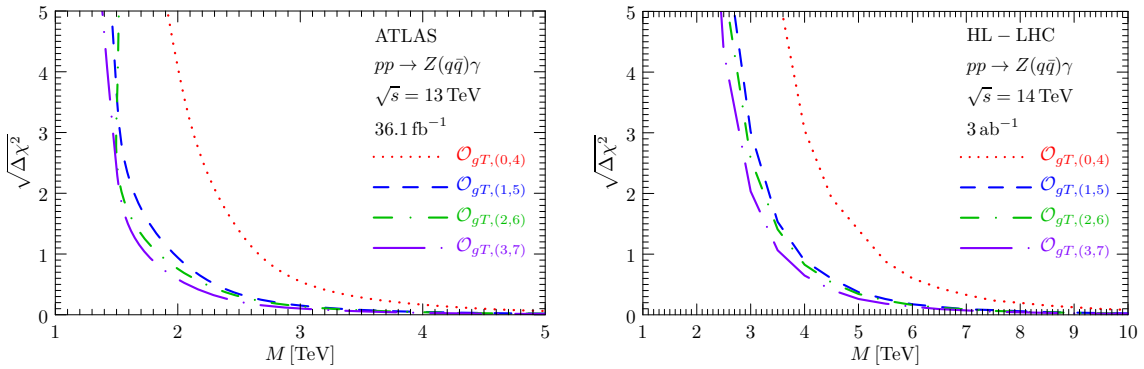

Figure 8. The significances $\sqrt{\Delta\chi^2}$ for probes of the individual dimension-8 gQGC operators $\mathcal{O}_{gT,(i,i+4)}$, where $i = 0, 1, 2, 3$, from the $Z(q\bar{q})\gamma$ channel as functions of the cut-off scales M_i. The left panel shows the sensitivities obtained using the current LHC data with $\sqrt{s} = 13\,\text{TeV}$ and luminosity $\mathcal{L} = 36.1\,\text{fb}^{-1}$ while the right panel shows the estimated sensitivities for the future HL-LHC with $\sqrt{s} = 14\,\text{TeV}$ and $\mathcal{L} = 3\,\text{ab}^{-1}$.

Process	25 TeV	50 TeV	100 TeV
$pp \to \gamma\gamma$	$p_{T,\gamma} = 100\,\text{GeV}$	$p_{T,\gamma} = 150\,\text{GeV}$	$p_{T,\gamma} = 300\,\text{GeV}$
$pp \to Z(\ell^+\ell^-)\gamma$	$p_{T,\gamma} = 60\,\text{GeV}$ $p_{T,\ell} = 50\,\text{GeV}$	$p_{T,\gamma} = 100\,\text{GeV}$ $p_{T,\ell} = 80\,\text{GeV}$	$p_{T,\gamma} = 200\,\text{GeV}$ $p_{T,\ell} = 160\,\text{GeV}$
$pp \to Z(\nu\bar{\nu})\gamma$	$p_{T,\gamma} = 250\,\text{GeV}$ $\not{p}_T = 250\,\text{GeV}$	$p_{T,\gamma} = 450\,\text{GeV}$ $\not{p}_T = 500\,\text{GeV}$	$p_{T,\gamma} = 1000\,\text{GeV}$ $\not{p}_T = 1000\,\text{GeV}$
$pp \to Z(q\bar{q})\gamma$	$p_{T,\gamma} = 400\,\text{GeV}$	$p_{T,\gamma} = 800\,\text{GeV}$	$p_{T,\gamma} = 1600\,\text{GeV}$

Table 1. Transverse momentum cuts at higher-energy colliders.

5 Prospective sensitivities at future hadron colliders

In addition to the existing LHC and its upgrade to HL-LHC, other hadronic colliders are being proposed, including HE-LHC [34], FCC-hh [39], and SppC [40], whose collision energies range from 25 TeV to 50 TeV and 100 TeV. As discussed in section 3.1, because of its strong momentum dependence, the gQGC signal increases very rapidly with the colliding energy. This gives future higher-energy hadron colliders great advantages for probing the gQGC operators. In addition, future hadron colliders typically have much larger luminosity than the current LHC. We assume a universal figure of $\mathcal{L} = 20\ \text{ab}^{-1}$ for the various higher-energy colliders and higher p_T cutoffs than for the LHC, as shown in table 1, but retain the same scattering-angle cuts as for the LHC.

Figure 9 compares the sensitivities at the LHC and possible future hadron colliders with centre-of-mass energies of (25, 50, and 100) TeV, characteristic of HE-LHC and FCC-hh/SppC. The sensitivities of the different colliders are colour-coded with shadings to distinguish the various final states considered. As expected, the higher the collision energy, the greater the sensitivity. The greatest $Z\gamma$ sensitivity is in general provided by $Z \to \nu\bar{\nu}$ decays, while the $\gamma\gamma$ channel provides even greater sensitivities for $\mathcal{O}_{gT,(4,5,6,7)}$.

JHEP04(2022)123

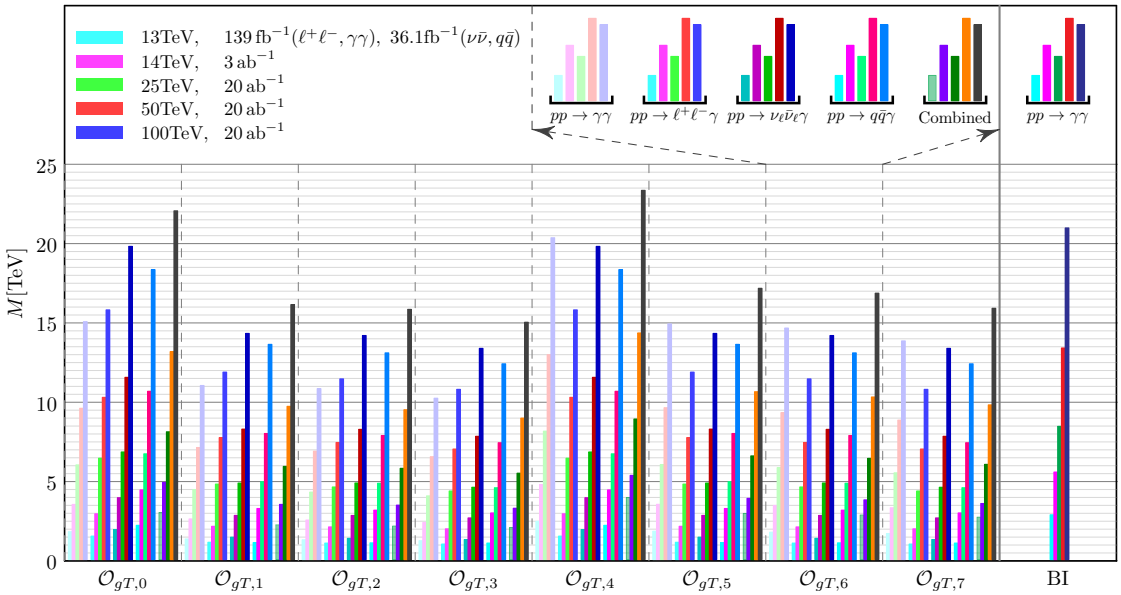

Figure 9. The 95% C.L. sensitivities of the various channels at the LHC, HL-LHC and proposed future hadron colliders, with cuts given in table 1.

We also show the combined sensitivities of the $Z\gamma$ and $\gamma\gamma$ channels by summing the χ^2 functions in figure 4, Figure 5, figure 6, and figure 8 for the LHC and similarly for the future higher-energy colliders. The lower bound at 95% C.L. can be significantly enhanced in 100 TeV collisions to above 20 TeV for $\mathcal{O}_{gT,(0,4)}$ and the SM Born-Infeld extension, an order of magnitude beyond the current LHC limits.

6 Potential improvements using the Z spin and angular correlation

As mentioned above, the $pp\to Z(\ell^+\ell^-,\bar{q}q)\gamma$ channels have three detectable particles in the final state. In these cases, not only the scattering angle distribution at the intermediate $Z\gamma$ level that is shown in figure 2 can be used for background discrimination, but also the difference between the $Z\gamma$ scattering plane and the decay plane of $Z\to\ell^+\ell^-,q\bar{q}$ can provide useful information. Thus the phenomenology of the $Z(\ell^+\ell^-,\bar{q}q)$ channels is in principle much richer than that for $pp\to\gamma\gamma$ and $pp\to Z(\nu\bar{\nu})\gamma$, which yield only photons in the final state. In this section we explore basic features of the Z spin and angular correlations with a view of potential improvements in the analysis sensitivity.

In order to keep full information on the $Z\to\ell^+\ell^-,q\bar{q}$ decays, we adopt the helicity amplitude formalism [41] to calculate the scattering matrix element for the $gg\to Z\gamma$ process:

$$g(\vec{p}_1,\lambda_1)+g(\vec{p}_2,\lambda_2)\quad\longrightarrow\quad Z^*(\vec{p}_Z,\lambda_Z)+\gamma(\vec{p}_\gamma,\lambda_\gamma) \tag{6.1a}$$

$$\hookrightarrow f(\vec{p}_f,\lambda_f)+\overline{f}(\vec{p}_{\bar{f}},\lambda_{\bar{f}})\,. \tag{6.1b}$$

Here, $\lambda_{1,2}=\pm1$ and $\lambda_\gamma=\pm1$ are the helicities of the massless gluons and photon, respectively, whereas in the case of the massive Z boson we have $\lambda_Z=0,\pm1$. Also,

JHEP04(2022)123

$\lambda_f/2 = \pm 1/2$ denote the helicities of the final-state fermions from Z decay. For simplicity, we assume that the masses of the final-state fermions can be neglected.

The amplitude for the two-step process of $Z\gamma$ production followed by Z boson decay can be written as

$$\mathcal{M} = \mathcal{D}_\mu(Z^* \to f + \overline{f})\mathcal{G}^{\mu\nu}(Z^*)\mathcal{P}_\nu(g + g \to Z^* + \gamma), \tag{6.2}$$

where $\mathcal{P}_\nu \equiv \langle Z^*_\mu\gamma|\mathcal{O}_i|g_1g_2\rangle$ and $\mathcal{D}_\mu \equiv \langle f\bar{f}|\mathcal{O}_{SM}|Z^*_\nu\rangle$ are the matrix elements for the production and decay of Z^*, respectively. The intermediate Z-boson propagator $\mathcal{G}^{\mu\nu}(Z^*)$ can be written as

$$\mathcal{G}^{\mu\nu}(Z^*) \equiv \frac{-(g^{\mu\nu} - p^\mu p^\nu/m_Z^2)}{\hat{s} - m_Z^2 + im\Gamma_Z}\,. \tag{6.3}$$

Since the decay width of the Z boson is considerably smaller than its mass, we use here the narrow-width approximation $(\hat{s} - m_Z^2 + im\Gamma_Z)\mathcal{G}^{\mu\nu}(Z^*) \approx \sum_{\lambda_Z} \epsilon^\mu_{\lambda_Z}(p)\epsilon^{\nu*}_{\lambda_Z}(p)$. Then one polarization vector $\epsilon^{\nu*}_{\lambda_Z}$ contracts with $\mathcal{P}_\nu$ to give the production matrix element while the other polarization vector $\epsilon^\mu_{\lambda_Z}$ contracts with $\mathcal{D}_\mu$ to give the decay matrix element. Consequently, the total helicity amplitude (6.2) can be decomposed into a sum of products of three scalars:

$$\mathcal{M} = D_Z^{-1}\sum_{\lambda_Z}\mathcal{P}_{\lambda_Z}\mathcal{D}_{\lambda_Z}\,, \tag{6.4}$$

where $D_Z \equiv \hat{s} - m_Z^2 + im_Z\Gamma_Z$. The summation is over the helicity of the internal Z boson, which does not change during free propagation. The production and decay matrix elements are

$$\mathcal{P}_{\lambda_Z} \equiv \mathcal{P}(g + g \to Z^* + \gamma)\cdot\epsilon^*_{\lambda_Z}(p)\,, \qquad \mathcal{D}_{\lambda_Z} \equiv \mathcal{D}(Z^* \to f + \overline{f}\,)\cdot\epsilon_{\lambda_Z}(p)\,, \tag{6.5}$$

which can be calculated in the usual way for $gg \to Z\gamma$ and $Z \to f\bar{f}$ separately.

The spin information appears in the absolute square of the scattering matrix element,

$$|\mathcal{M}|^2 = |D_Z|^{-2}\sum_{\lambda_Z}\sum_{\lambda'_Z}\mathcal{P}^{\lambda'_Z}_{\lambda_Z}\mathcal{D}^{\lambda'_Z}_{\lambda_Z}\,, \tag{6.6}$$

where

$$\mathcal{P}^{\lambda'_Z}_{\lambda_Z} \equiv \mathcal{P}_{\lambda_Z}(\mathcal{P}_{\lambda'_Z})^\dagger = \mathcal{P}_\mu\mathcal{P}^\dagger_\nu\,\epsilon^{\mu*}_{\lambda_Z}(p)\,\epsilon^\nu_{\lambda'_Z}(p) \equiv \mathcal{P}_{\mu\nu}\,\epsilon^{\mu*}_{\lambda_Z}(p)\,\epsilon^\nu_{\lambda'_Z}(p)\,, \tag{6.7a}$$

$$\mathcal{D}^{\lambda'_Z}_{\lambda_Z} \equiv \mathcal{D}_{\lambda_Z}(\mathcal{D}_{\lambda'_Z})^\dagger = \mathcal{D}_\mu\mathcal{D}^\dagger_\nu\,\epsilon^{\mu*}_{\lambda_Z}(p)\,\epsilon^\nu_{\lambda'_Z}(p) \equiv \mathcal{D}_{\mu\nu}\,\epsilon^\mu_{\lambda_Z}(p)\,\epsilon^{\nu*}_{\lambda'_Z}(p)\,, \tag{6.7b}$$

The Z-boson polarization vectors encode the spin information.

Resolving the decay plane of the channel $Z \to \bar{\nu}\nu$ is not possible, and resolving that of $Z \to \bar{q}q$ is challenging in practice, particularly when the Z boson is highly boosted. Therefore here we investigate in detail only the leptonic decay channel. The Z-boson momentum provides a natural definition of the z-axis with respect to which we define the fermion polar angle $\theta^\star_\ell$ in the Z rest frame. Since the detector is azimuthally symmetric,

JHEP04(2022)123

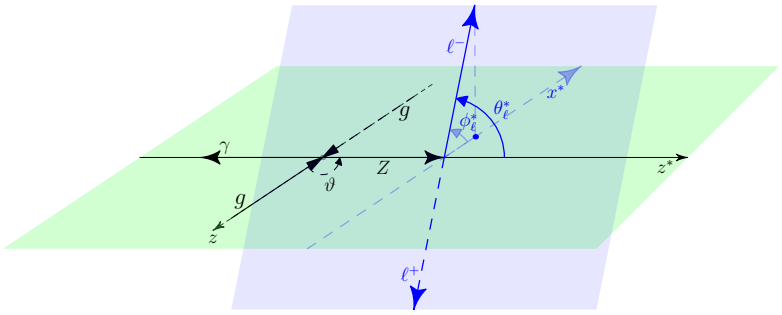

Figure 10. Kinematic variables for the process $gg \to Z(f\bar{f})\gamma$. The scattering plane is defined by the incoming gluons and outgoing Z/γ bosons. The polar angle (scattering angle) of the Z boson is defined as ϑ, $\vec{z}^*$ is defined as the $\hat{z}^*$-axis in the rest frame of the Z boson along the direction of the Z boson momentum, and the $\hat{x}^* - \hat{z}^*$ plane is spanned by the vector $\vec{z}^*$ and the direction of the initial gluon motion. The polar and azimuthal angles of the leptons in the rest frame of the Z boson are θ^*_ℓ and ϕ^*_ℓ.

we can without loss of generality define the $\hat{x}$-axis to lie in the scattering plane of the Z and γ bosons, with the Z momentum having a positive $\hat{x}$ component. The azimuthal angle difference between the scattering and decay planes is $\phi^\star_\ell$, see figure 10. Then the decay polarization tensor components $\mathcal{D}^{\lambda'_Z}_{\lambda_Z}$ are

$$\mathcal{D}^{\pm}_{\pm} = m_Z^2 \Big[\left(g_V^2 + g_A^2\right) \left(1 + \cos^2\theta^\star_\ell\right) \pm 4 g_V g_A \cos\theta^\star_\ell \Big] , \tag{6.8a}$$

$$\mathcal{D}^{0}_{0} = 2m_Z^2 \left(g_V^2 + g_A^2\right) \sin^2\theta^\star_\ell , \tag{6.8b}$$

$$\mathcal{D}^{\mp}_{\pm} = m_Z^2 \left(g_V^2 + g_A^2\right) \sin^2\theta^\star_\ell e^{\pm i 2\phi^\star_\ell} , \tag{6.8c}$$

$$\mathcal{D}^{0}_{\pm} = \frac{\pm 1}{\sqrt{2}} m_Z^2 \Big[\left(g_V^2 + g_A^2\right) \sin(2\theta^\star_\ell) \pm 4 g_V g_A \sin\theta^\star_\ell \Big] e^{\pm i\phi^\star_\ell} . \tag{6.8d}$$

The polarization state of the intermediate Z boson depends in general on the dimension-8 gQGC operators that produces it, carrying information beyond that provided by its momentum.[3] The decays of the Z boson open a window on the polarization information. Below we show how to use the fermion polar angle in section 6.1 and the azimuthal angle in section 6.2 to distinguish the gQGC operators. With enough event rate, it is also possible to study a combined two-dimensional distribution of polar and azimuthal angles as we discuss in section 6.3.

6.1 Polarization effects in the fermion polar angle distribution

The Z polarization tensor $\mathcal{P}^{\lambda'_Z}_{\lambda_Z}$ is defined in the laboratory frame with the z-axis along the beam direction. Since the scattering is rotationally-invariant with respect to the azimuthal

[3] In principle this also applies to the associated photon, but it is so energetic that its polarization cannot be easily extracted.

JHEP04(2022)123

angle, the components of $\mathcal{P}^{\lambda'_Z}_{\lambda_Z}$ depend only on the scattering angle ϑ:

$$(\mathcal{P}_{0,4})^{\pm}_{\pm} = \frac{4s_w c_w}{16^2 M_i^8}\frac{\hat{s}^4}{256}(1-x_Z)^2\Big[64\Big]\,, \tag{6.9a}$$

$$(\mathcal{P}_{0,4})^{0}_{0} = 0\,, \tag{6.9b}$$

$$(\mathcal{P}_{1,5})^{\pm}_{\pm} = \frac{4s_w c_w}{16^2 M_i^8}\frac{\hat{s}^4}{256}(1-x_Z)^2\Big[292+208\cos(2\vartheta)+12\cos(4\vartheta)+96x_Z^2\sin^4\vartheta\Big]\,, \tag{6.9c}$$

$$(\mathcal{P}_{1,5})^{0}_{0} = \frac{4s_w c_w}{16^2 M_i^8}\frac{\hat{s}^4}{256}(1-x_Z)^2\Big[64\,x_Z\sin^2\vartheta(5+3\cos(2\vartheta))\Big]\,, \tag{6.9d}$$

$$(\mathcal{P}_{2,6})^{\pm}_{\pm} = \frac{4s_w c_w}{16^2 M_i^8}\frac{\hat{s}^4}{256}(1-x_Z)^2\Big[163+28\cos(2\vartheta)+\cos(4\vartheta)+8x_Z^2\sin^4\vartheta\Big]\,, \tag{6.9e}$$

$$(\mathcal{P}_{2,6})^{0}_{0} = \frac{4s_w c_w}{16^2 M_i^8}\frac{\hat{s}^4}{256}(1-x_Z)^2\Big[16\,x_Z\sin^2\vartheta(3+\cos(2\vartheta))\Big]\,, \tag{6.9f}$$

$$(\mathcal{P}_{3,7})^{\pm}_{\pm} = \frac{4s_w c_w}{16^2 M_i^8}\frac{\hat{s}^4}{256}(1-x_Z)^2\Big[105+20\cos(2\vartheta)+3\cos(4\vartheta)+24x_Z^2\sin^4\vartheta\Big]\,, \tag{6.9g}$$

$$(\mathcal{P}_{3,7})^{0}_{0} = \frac{4s_w c_w}{16^2 M_i^8}\frac{\hat{s}^4}{256}(1-x_Z)^2\Big[16\,x_Z\sin^2\vartheta(5+3\cos(2\vartheta))\Big]\,, \tag{6.9h}$$

for the 8 gQGC operators. We see that the positive ($\lambda_Z = +$) and negative ($\lambda_Z = -$) polarization states are always produced equally. In other words, there is no net polarization effect. Furthermore, the production rate of the longitudinal state ($\lambda_Z = 0$) is suppressed by x_Z at large invariant mass $m_{Z\gamma}$, and therefore can be neglected at high-energy hadron colliders. However, in the region $x_Z \sim \mathcal{O}(1)$ it could be useful for distinguishing different Lorentz structures.

In the presence of the longitudinal mode, there is in principle a polarization effect, though its magnitude decreases with increasing center-of-mass energy $m_{Z\gamma}$. The polarization of the Z boson can be measured by studying angular distributions of its decay products. The differential cross sections with respect to the polar angle of the outgoing lepton are given by

$$\frac{d\sigma_{\gamma\ell^+\ell^-,(0,4)}}{\sigma_{\gamma\ell^+\ell^-,0,4}\,d\cos\theta^\star_\ell} = \frac{3}{8}\left(1+\cos^2\theta^\star_\ell\right)\,, \tag{6.10a}$$

$$\frac{d\sigma_{\gamma\ell^+\ell^-,(1,5)}}{\sigma_{\gamma\ell^+\ell^-,1,5}\,d\cos\theta^\star_\ell} = \frac{3\left[26(1+\cos^2\theta^\star_\ell)+16x_Z\sin^2\theta^\star_\ell+3x_Z^2\cos(2\theta^\star_\ell)+9x_Z^2\right]}{16\left(13+4x_Z+3x_Z^2\right)}\,, \tag{6.10b}$$

$$\frac{d\sigma_{\gamma\ell^+\ell^-,(2,6)}}{\sigma_{\gamma\ell^+\ell^-,2,6}\,d\cos\theta^\star_\ell} = \frac{3\left[72(1+\cos^2\theta^\star_\ell)+12x_Z\sin^2\theta^\star_\ell+x_Z^2\cos(2\theta^\star_\ell)+3x_Z^2\right]}{16\left(36+3x_Z+x_Z^2\right)}\,, \tag{6.10c}$$

$$\frac{d\sigma_{\gamma\ell^+\ell^-,(3,7)}}{\sigma_{\gamma\ell^+\ell^-,3,7}\,d\cos\theta^\star_\ell} = \frac{3\left[46(1+\cos^2\theta^\star_\ell)+16x_Z\sin^2\theta^\star_\ell+3x_Z^2\cos(2\theta^\star_\ell)+9x_Z^2\right]}{16\left(23+4x_Z+3x_Z^2\right)}\,. \tag{6.10d}$$

For $\mathcal{O}_{gT,(0,4)}$, since the Z boson is generated isotropically as shown in figure 2, the polar angle of the lepton is identical with the distribution in the decay of an unpolarized Z boson. However, the situations for other operators differ because of the contributions of the longitudinal component. The left panel of figure 11 shows the normalized differential cross

JHEP04(2022)123

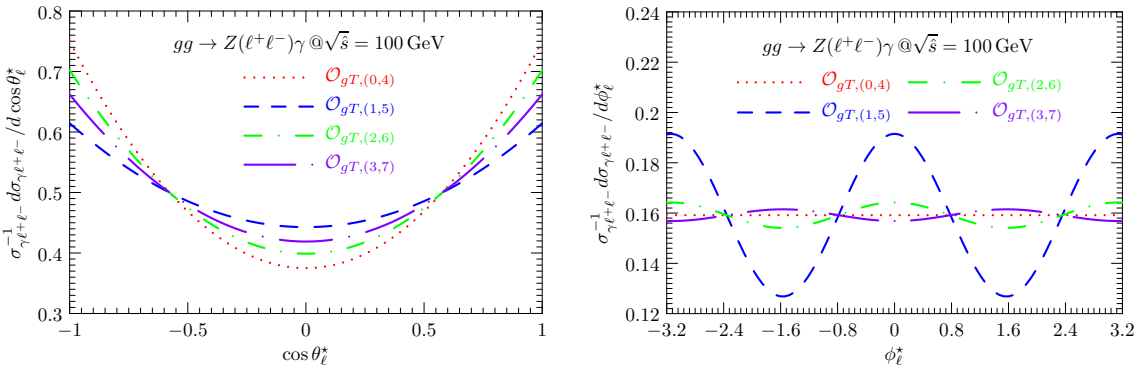

Figure 11. The normalized differential cross sections in the polar ($\theta^\star_\ell$) and azimuthal ($\phi^\star_\ell$) angles of the outgoing lepton when the gluon-gluon collision energy $\sqrt{\hat{s}} = 100\,\text{GeV}$.

sections at the gluon-gluon collision energy $\sqrt{\hat{s}} = 100\,\text{GeV}$, where sizeable differences can appear. However, these differences are proportional to the scale factor x_Z, and in the limit $x_Z \to 0$ all the curves in the left panel of figure 11 converge to forms $\propto 1 + \cos^2\theta^\star_\ell$.

6.2 Spin correlation in fermion azimuthal angle distributions

Since the intermediate Z is not directly measured, it is in general produced in an entangled spin state with the only exception being when produced by the operators $\mathcal{O}_{gT,(0,4)}$. Hence different polarizations correlates with each other and the interference between the helicity states can induce non-trivial distributions of the fermion azimuthal angle. To make this transparent, it is necessary to calculate the relevant off-diagonal matrix elements of the $gg \to Z\gamma$ production process:

$$(\mathcal{P}_{0,4})^{\mp}_{\pm} = 0\,, \tag{6.11a}$$

$$(\mathcal{P}_{1,5})^{\mp}_{\pm} = \frac{4c_w s_w}{16^2}\frac{12}{32}\frac{\hat{s}^4}{M_i^8} x_Z\,(1-x_Z)^2\,[3+\cos(2\vartheta)]\sin^2\vartheta\,, \tag{6.11b}$$

$$(\mathcal{P}_{2,6})^{\mp}_{\pm} = \frac{4c_w s_w}{16^2}\frac{1}{32}\frac{\hat{s}^4}{M_i^8} x_Z(1-x_Z)^2\,[3+2\cos(2\vartheta)]\sin^2\vartheta\,, \tag{6.11c}$$

$$(\mathcal{P}_{3,7})^{\mp}_{\pm} = \frac{4c_w s_w}{16^2}\frac{1}{32}\frac{\hat{s}^4}{M_i^8} x_Z(1-x_Z)^2\,[1+3\cos(2\vartheta)]\sin^2\vartheta\,. \tag{6.11d}$$

The related off-diagonal matrix elements of the $Z \to \ell^+\ell^-$ decay process are given in (6.8c) and (6.8d). We see that the transverse-transverse correlation effect leads to a non-trivial dependence on the azimuthal angle $\phi^\star_\ell$ of the outgoing lepton. The normalized differential cross sections with respect to the azimuthal angle of the outgoing lepton for the different

JHEP04(2022)123

operators are

$$\frac{d\sigma_{\gamma\ell^+\ell^-,0,4}}{\sigma_{\gamma\ell^+\ell^-,0,4}\,d\phi_\ell^\star} = \frac{1}{2\pi}\,, \tag{6.12a}$$

$$\frac{d\sigma_{\gamma\ell^+\ell^-,1,5}}{\sigma_{\gamma\ell^+\ell^-,1,5}\,d\phi_\ell^\star} = \frac{26+6x_Z^2+8x_Z+9x_Z\cos(2\phi_\ell^\star)}{4\pi\,(3x_Z^2+4x_Z+13)}\,, \tag{6.12b}$$

$$\frac{d\sigma_{\gamma\ell^+\ell^-,2,6}}{\sigma_{\gamma\ell^+\ell^-,2,6}\,d\phi_\ell^\star} = \frac{72+2x_Z^2+6x_Z+3x_Z\cos(2\phi_\ell^\star)}{4\pi\,(x_Z^2+3x_Z+36)}\,, \tag{6.12c}$$

$$\frac{d\sigma_{\gamma\ell^+\ell^-,3,7}}{\sigma_{\gamma\ell^+\ell^-,3,7}\,d\phi_\ell^\star} = \frac{46+6x_Z^2+8x_Z-x_Z\cos(2\phi_\ell^\star)}{4\pi\,(3x_Z^2+4x_Z+23)}\,. \tag{6.12d}$$

A non-trivial distribution of the azimuthal angle ϕ_ℓ^* would indicate the importance of a gQGC operator different from $\mathcal{O}_{gT,(0,4)}$, offering in principle the possibility of distinguishing the gQGC operators. The right panel of figure 11 shows the normalized differential cross sections at a gluon-gluon collision energy $\sqrt{\hat{s}} = 100\,\text{GeV}$. We see that, compared to the polarization effect in the left panel of figure 11, the correlation effect is expected to be more sensitive to the Lorentz structures of the gQGC operators. However, the effect is suppressed by x_Z at high $M_{Z\gamma}$.

6.3 Combined distribution of scattering and azimuthal angles

A non-trivial azimuthal angle distribution was also searched for by ATLAS [20]. As shown in the previous section, the spin correlation in the lepton azimuthal angle distribution is due to the off-diagonal elements eq. (6.11) in Z production. We observe that these off-diagonal elements have non-trivial dependence on the Z boson scattering angle ϑ. More spin information can in principle be extracted from the correlation between the Z scattering angle ϑ and the lepton azimuthal angle ϕ_ℓ^*. The corresponding normalized double differential cross sections for the gQGC operators are

$$\frac{d\sigma_{\gamma\ell^+\ell^-,0,4}}{\sigma_{\gamma\ell^+\ell^-,0,4}\,d\cos\vartheta d\phi_\ell^\star} = \frac{1}{4\pi}\,,$$

$$\begin{aligned}\frac{d\sigma_{\gamma\ell^+\ell^-,1,5}}{\sigma_{\gamma\ell^+\ell^-,1,5}\,d\cos\vartheta d\phi_\ell^\star} = \frac{15}{256\pi\,(3x_Z^2+4x_Z+13)}\Big[&73+52\cos(2\vartheta)+3\cos(4\vartheta)\,,\\ &+24\sin^4(\vartheta)x_Z^2+40\sin^2(\vartheta)x_Z+24\sin^2(\vartheta)\cos(2\vartheta)x_Z\\ &+12\sin^2(\vartheta)\cos(2\vartheta)x_Z\cos(2\phi_\ell^\star)+36\sin^2(\vartheta)x_Z\cos(2\phi_\ell^\star)\Big]\,,\end{aligned} \tag{6.13a}$$

$$\begin{aligned}\frac{d\sigma_{\gamma\ell^+\ell^-,2,6}}{\sigma_{\gamma\ell^+\ell^-,2,6}\,d\cos\vartheta d\phi_\ell^\star} = \frac{15}{256\pi\,(x_Z^2+3x_Z+36)}\Big[&163+28\cos(2\vartheta)+\cos(4\vartheta)\\ &+8\sin^4(\vartheta)x_Z^2+24\sin^2(\vartheta)x_Z+8\sin^2(\vartheta)\cos(2\vartheta)x_Z\\ &+4\sin^2(\vartheta)\cos(2\vartheta)x_Z\cos(2\phi_\ell^\star)+12\sin^2(\vartheta)x_Z\cos(2\phi_\ell^\star)\Big]\,,\end{aligned} \tag{6.13b}$$

$$\begin{aligned}\frac{d\sigma_{\gamma\ell^+\ell^-,3,7}}{\sigma_{\gamma\ell^+\ell^-,3,7}\,d\cos\vartheta d\phi_\ell^\star} = \frac{15}{256\pi\,(3x_Z^2+4x_Z+23)}\Big[&105+20\cos(2\vartheta)+3\cos(4\vartheta)\\ &+24x_Z\sin^2(\vartheta)\cos(2\vartheta)+24\sin^4(\vartheta)x_Z^2+40\sin^2(\vartheta)x_Z\\ &+12x_Z\sin^2(\vartheta)\cos(2\vartheta)\cos(2\phi_\ell^\star)+4x_Z\sin^2(\vartheta)\cos(2\phi_\ell^\star)\Big]\,.\end{aligned} \tag{6.13c, 6.13d}$$

JHEP04(2022)123

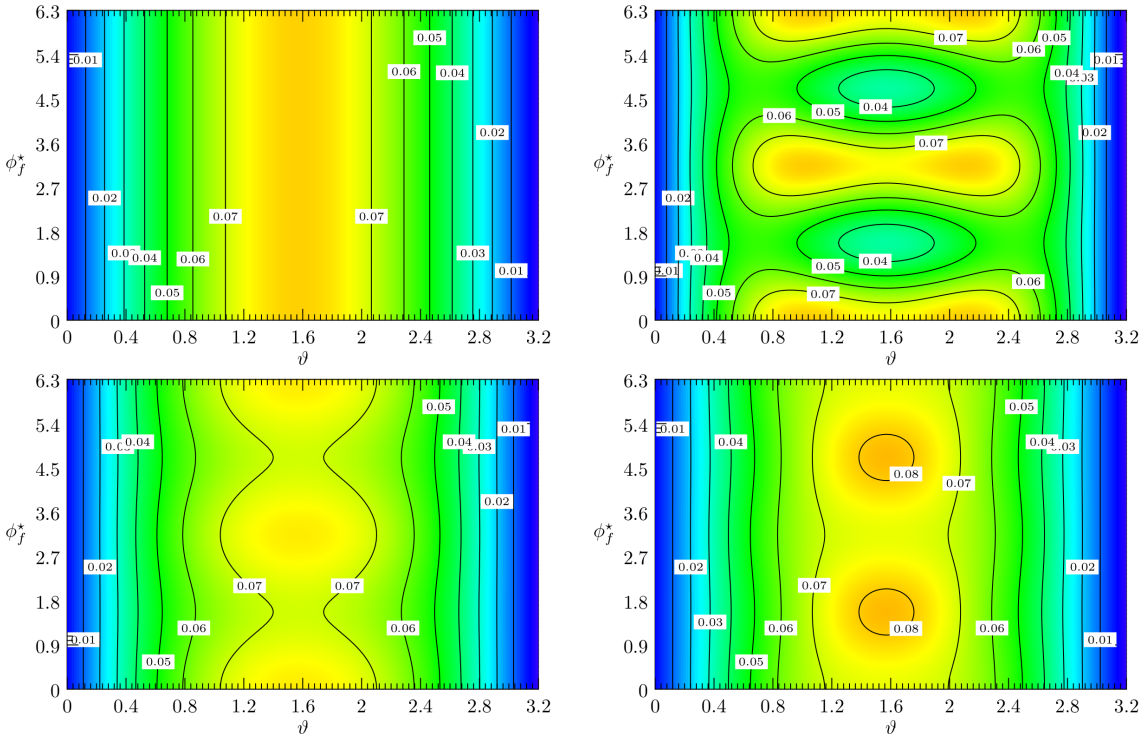

Figure 12. Contour plots in the plane of the lepton azimuthal angle $\phi_\ell^\star$ and the Z boson polar angle ϑ for the gQGC operators $\mathcal{O}_{gT,(0,4)}$ (upper left), $\mathcal{O}_{gT,(1,5)}$ (upper right), $\mathcal{O}_{gT,(2,6)}$ (lower left), and $\mathcal{O}_{gT,(3,7)}$ (lower right). These results are for a gluon-gluon collision energy $\sqrt{\hat{s}} = 100\,\text{GeV}$.

Figure 12 shows contours of the normalized double-differential cross section at the gluon-gluon collision energy $\sqrt{\hat{s}} = 100\,\text{GeV}$. We see that the angles ϑ and ϕ_ℓ^* are correlated very differently for different Lorentz structures, but note that the transverse-transverse correlation effects also depend on x_Z. In particular, for $\mathcal{O}_{gT,(0,4)}$ and $\mathcal{O}_{gT,(3,7)}$, the polar angle ϑ distributions (at $\sqrt{\hat{s}} = 100\,\text{GeV}$) are very similar but the $\phi_\ell^\star$ correlation properties are very different. Thus the two-dimensional distribution carries additional information beyond that provided by the one-dimensional distributions.

7 Conclusions

The SMEFT is a powerful way of searching for possible indirect effects of new physics beyond the SM that may appear at energies outside the direct reaches of active experiments. In particular, the SMEFT provides a framework for exploring possible anomalous multi-boson couplings while taking into account all the gauge symmetries of the SM, which is one of the priority measurements for LHC and possible future colliders. The present and prospective experimental sensitivities to anomalous triple gauge couplings (TGCs) and quartic gauge couplings (QGCs) have been studied extensively, but there have been fewer studies of possible quartic couplings between gluons and electroweak gauge bosons, which are absent in the SM. In the SMEFT, these are first generated by dimension-8 operators, whose

JHEP04(2022)123

study offers an interesting window on BSM physics [7], complementing the exploration of dimension-6 operators that have been analyzed extensively, see [4, 5] and references therein.

In this paper we have presented a first analysis of the experimental sensitivities of measurements of the $gg \to Z\gamma$ process to the dimension-8 quartic couplings of pairs of gluons to the Z and photon (gQGCs), including an analysis of present LHC data and assessments of the prospects at HL-LHC and proposed higher-energy proton-proton colliders. Four distinct Lorentz structures of CP-conserving dimension-8 operators contain gQGCs, and each may be constructed either with pairs of SU(2) or U(1) gauge field strengths. We have stressed the differences between the polar angle distributions they generate from the one generated by the dominant SM background due to $\bar{q}q \to Z\gamma$, and analyzed the possible sensitivities of analyses of $Z \to \ell^+\ell^-, \bar{\nu}\nu$ and $\bar{q}q$ final states. The present LHC data on these final states correspond to integrated luminosities up to $139\,\text{fb}^{-1}$ at 13 TeV, and we show that they exclude mass scales $\lesssim 2$ TeV in the dimension-8 operator coefficients, with future colliders offering sensitivities to scales an order of magnitude higher, extending above 20 TeV for $\mathcal{O}_{gT,(0,4)}$. The $gg \to ZZ$ channel has more complex phenomenology that will be studied in a separate paper.

We also present an updated analysis of the sensitivities of LHC measurements of the $\gamma\gamma$ final state with up to $139\,\text{fb}^{-1}$ at 13 TeV and at future colliders. The present data already constrain the nonlinearity scale of the Born-Infeld extension of the SM to be $\gtrsim 5$ TeV, putting pressure on some brane models that address the electroweak hierarchy problem. A future collider with 100 TeV in the center of mass could be sensitive to Born-Infeld scales $\gtrsim 20$ TeV. As we also show, potential analysis improvements might be made possible by exploiting Z spin measurements and angular correlations using decays into $\ell^+\ell^-$ and $\bar{q}q$ final states, which are important at low $Z\gamma$ invariant masses.

Our results provide further illustrations of possibilities for exploring and constraining possible dimension-8 terms in the SMEFT, in addition to light-by-light scattering [6, 18] and the searches for neutral triple-gauge couplings discussed elsewhere [8, 9]. There is plenty of life in the SMEFT beyond dimension 6.

Acknowledgments

The work of J.E. was supported partly by the United Kingdom STFC Grant ST/T000759/1 and partly by the Estonian Research Council via a Mobilitas Pluss grant. This work was supported by the Double First Class start-up fund (WF220442604), the Shanghai Pujiang Program (20PJ1407800), and National Natural Science Foundation of China (No. 12090064). This work was also supported in part by Chinese Academy of Sciences Center for Excellence in Particle Physics (CCEPP). K.M. was supported by the Innovation Capability Support Program of Shaanxi (Program No. 2021KJXX-47), as well as the Visitor Program of Shanghai Jiao Tong University.

JHEP04(2022)123

References

[1] I. Brivio et al., *Disentangling a dynamical Higgs*, *JHEP* **03** (2014) 024 [arXiv:1311.1823] [INSPIRE].

[2] D.R. Green, P. Meade and M.-A. Pleier, *Multiboson interactions at the LHC*, *Rev. Mod. Phys.* **89** (2017) 035008 [arXiv:1610.07572] [INSPIRE].

[3] M. Rauch, *Vector-Boson Fusion and Vector-Boson Scattering*, arXiv:1610.08420 [INSPIRE].

[4] J. Ellis, M. Madigan, K. Mimasu, V. Sanz and T. You, *Top, Higgs, Diboson and Electroweak Fit to the Standard Model Effective Field Theory*, *JHEP* **04** (2021) 279 [arXiv:2012.02779] [INSPIRE].

[5] SMEFiT collaboration, *Combined SMEFT interpretation of Higgs, diboson, and top quark data from the LHC*, *JHEP* **11** (2021) 089 [arXiv:2105.00006] [INSPIRE].

[6] J. Ellis, N.E. Mavromatos and T. You, *Light-by-Light Scattering Constraint on Born-Infeld Theory*, *Phys. Rev. Lett.* **118** (2017) 261802 [arXiv:1703.08450] [INSPIRE].

[7] J. Ellis and S.-F. Ge, *Constraining Gluonic Quartic Gauge Coupling Operators with $gg \to \gamma\gamma$*, *Phys. Rev. Lett.* **121** (2018) 041801 [arXiv:1802.02416] [INSPIRE].

[8] J. Ellis, S.-F. Ge, H.-J. He and R.-Q. Xiao, *Probing the scale of new physics in the $ZZ\gamma$ coupling at e^+e^- colliders*, *Chin. Phys. C* **44** (2020) 063106 [arXiv:1902.06631] [INSPIRE].

[9] J. Ellis, H.-J. He and R.-Q. Xiao, *Probing new physics in dimension-8 neutral gauge couplings at e^+e^- colliders*, *Sci. China Phys. Mech. Astron.* **64** (2021) 221062 [arXiv:2008.04298] [INSPIRE].

[10] W. Heisenberg and H. Euler, *Consequences of Dirac's theory of positrons*, *Z. Phys.* **98** (1936) 714 [physics/0605038] [INSPIRE].

[11] D. Bardin, L. Kalinovskaya and E. Uglov, *Standard Model light-by-light scattering in SANC: analytic and numeric evaluation*, *Phys. Atom. Nucl.* **73** (2010) 1878 [arXiv:0911.5634] [INSPIRE].

[12] M. Born and L. Infeld, *Foundations of the new field theory*, *Proc. Roy. Soc. Lond. A* **144** (1934) 425 [INSPIRE].

[13] E.S. Fradkin and A.A. Tseytlin, *Nonlinear Electrodynamics from Quantized Strings*, *Phys. Lett. B* **163** (1985) 123 [INSPIRE].

[14] A.A. Tseytlin, *Born-Infeld action, supersymmetry and string theory*, in *The Many Faces of the Superworld*, pp. 417–452 (2000) [DOI] [hep-th/9908105] [INSPIRE].

[15] C. Cheung, K. Kampf, J. Novotny, C.-H. Shen, J. Trnka and C. Wen, *Vector Effective Field Theories from Soft Limits*, *Phys. Rev. Lett.* **120** (2018) 261602 [arXiv:1801.01496] [INSPIRE].

[16] ATLAS collaboration, *Evidence for light-by-light scattering in heavy-ion collisions with the ATLAS detector at the LHC*, *Nature Phys.* **13** (2017) 852 [arXiv:1702.01625] [INSPIRE].

[17] CMS collaboration, *Evidence for light-by-light scattering and searches for axion-like particles in ultraperipheral PbPb collisions at $\sqrt{s_{\rm NN}} = 5.02$ TeV*, *Phys. Lett. B* **797** (2019) 134826 [arXiv:1810.04602] [INSPIRE].

[18] TOTEM and CMS collaborations, *First search for exclusive diphoton production at high mass with tagged protons in proton-proton collisions at $\sqrt{s} = 13$ TeV*, arXiv:2110.05916 [INSPIRE].

JHEP04(2022)123

[19] ATLAS collaboration, *Search for new phenomena in high-mass diphoton final states using 37 fb^{-1} of proton-proton collisions collected at $\sqrt{s} = 13$ TeV with the ATLAS detector*, *Phys. Lett. B* **775** (2017) 105 [arXiv:1707.04147] [INSPIRE].

[20] ATLAS collaboration, *Measurement of the $Z(\to \ell^+\ell^-)\gamma$ production cross-section in pp collisions at $\sqrt{s} = 13$ TeV with the ATLAS detector*, *JHEP* **03** (2020) 054 [arXiv:1911.04813] [INSPIRE].

[21] ATLAS collaboration, *Measurement of the $Z\gamma \to \nu\bar{\nu}\gamma$ production cross section in pp collisions at $\sqrt{s} = 13$ TeV with the ATLAS detector and limits on anomalous triple gauge-boson couplings*, *JHEP* **12** (2018) 010 [arXiv:1810.04995] [INSPIRE].

[22] ATLAS collaboration, *Search for heavy resonances decaying to a photon and a hadronically decaying $Z/W/H$ boson in pp collisions at $\sqrt{s} = 13$ TeV with the ATLAS detector*, *Phys. Rev. D* **98** (2018) 032015 [arXiv:1805.01908] [INSPIRE].

[23] W. Buchmüller and D. Wyler, *Effective Lagrangian Analysis of New Interactions and Flavor Conservation*, *Nucl. Phys. B* **268** (1986) 621 [INSPIRE].

[24] C. Garcia-Garcia, M. Herrero and R.A. Morales, *Unitarization effects in EFT predictions of WZ scattering at the LHC*, *Phys. Rev. D* **100** (2019) 096003 [arXiv:1907.06668] [INSPIRE].

[25] K. Arnold et al., *VBFNLO: A Parton level Monte Carlo for processes with electroweak bosons*, *Comput. Phys. Commun.* **180** (2009) 1661 [arXiv:0811.4559] [INSPIRE].

[26] J.M. Cornwall, D.N. Levin and G. Tiktopoulos, *Derivation of Gauge Invariance from High-Energy Unitarity Bounds on the s Matrix*, *Phys. Rev. D* **10** (1974) 1145 [*Erratum ibid.* **11** (1975) 972] [INSPIRE].

[27] J. Ohnemus, *Order $\alpha^- s$ calculations of hadronic $W^\pm\gamma$ and $Z\gamma$ production*, *Phys. Rev. D* **47** (1993) 940 [INSPIRE].

[28] J. Alwall et al., *The automated computation of tree-level and next-to-leading order differential cross sections, and their matching to parton shower simulations*, *JHEP* **07** (2014) 079 [arXiv:1405.0301] [INSPIRE].

[29] A. Alloul, N.D. Christensen, C. Degrande, C. Duhr and B. Fuks, *FeynRules 2.0 — A complete toolbox for tree-level phenomenology*, *Comput. Phys. Commun.* **185** (2014) 2250 [arXiv:1310.1921] [INSPIRE].

[30] C. Degrande, C. Duhr, B. Fuks, D. Grellscheid, O. Mattelaer and T. Reiter, *UFO — The Universal FeynRules Output*, *Comput. Phys. Commun.* **183** (2012) 1201 [arXiv:1108.2040] [INSPIRE].

[31] S.-F. Ge, K. Hagiwara, N. Okamura and Y. Takaesu, *Determination of mass hierarchy with medium baseline reactor neutrino experiments*, *JHEP* **05** (2013) 131 [arXiv:1210.8141] [INSPIRE].

[32] S.-F. Ge, H.-J. He and R.-Q. Xiao, *Probing new physics scales from Higgs and electroweak observables at e^+e^- Higgs factory*, *JHEP* **10** (2016) 007 [arXiv:1603.03385] [INSPIRE].

[33] ATLAS collaboration, *Measurement of the production cross section of pairs of isolated photons in pp collisions at 13 TeV with the ATLAS detector*, *JHEP* **11** (2021) 169 [arXiv:2107.09330] [INSPIRE].

[34] X. Cid Vidal et al., *Report from Working Group 3*: Beyond the Standard Model physics at the HL-LHC and HE-LHC, *CERN Yellow Rep. Monogr.* **7** (2019) 585 [arXiv:1812.07831] [INSPIRE].

JHEP04(2022)123

[35] T. Sjöstrand et al., *An introduction to PYTHIA 8.2*, *Comput. Phys. Commun.* **191** (2015) 159 [arXiv:1410.3012] [INSPIRE].

[36] DELPHES 3 collaboration, *DELPHES 3, A modular framework for fast simulation of a generic collider experiment*, *JHEP* **02** (2014) 057 [arXiv:1307.6346] [INSPIRE].

[37] M. Cacciari, G.P. Salam and G. Soyez, *FastJet User Manual*, *Eur. Phys. J. C* **72** (2012) 1896 [arXiv:1111.6097] [INSPIRE].

[38] R. Brun and F. Rademakers, *ROOT: An object oriented data analysis framework*, *Nucl. Instrum. Meth. A* **389** (1997) 81 [INSPIRE].

[39] FCC collaboration, *FCC-hh: The Hadron Collider*: Future Circular Collider Conceptual Design Report Volume 3, *Eur. Phys. J. ST* **228** (2019) 755 [INSPIRE].

[40] M. Ahmad et al. *CEPC-SPPC Preliminary Conceptual Design Report. 1. Physics and Detector*, IHEP-CEPC-DR-2015-01 (2015) [INSPIRE].

[41] H. Murayama, I. Watanabe and K. Hagiwara, *HELAS: HELicity amplitude subroutines for Feynman diagram evaluations*, KEK-91-11 (1992) [INSPIRE].

[42] R. Frederix, S. Frixione, V. Hirschi, D. Pagani, H.S. Shao and M. Zaro, *The automation of next-to-leading order electroweak calculations*, *JHEP* **07** (2018) 185 [*Erratum ibid.* **11** (2021) 085] [arXiv:1804.10017] [INSPIRE].

JHEP04(2022)123